Chapter 1

Introduction

1.1 Hybrid Organic/Inorganic Light Emitting Devices

1.1.1 Inorganic Colloidal Semiconductor Nanocrystals

Inorganic Colloidal semiconductor nanocrystals (NCs) are nanometer sized, crystalline, a great number of semiconductor materials that can be fabricated in solution due to molecules bound to the quantum dots (QDs) surface maintaining favorable NC/solvent interactions (Figure 1.1a). The smallest QDs are nearly molecular (< 100 atoms), while the largestare consist of over 100,000 atoms. This size lies in between molecular and bulk semiconductor material is characterized by optical properties of the semiconductor due to quantum confinement effect[1], which comes about when the dimensions of lots of semiconductor become so small that the photoexcited carriers feel the boundaries.

The size between 2 to 15 nm in diameter of NCs is on the order of the size of the Bohr radius of the bulk exciton (i.e. 5.6 nm for CdSe)[2]. Photoexcitation or electrical excitation of the NCs creates an electron-hole pair that is confined to and delocalized over the entire volume of the NC, which confines the exciton in all three dimensions and causes the continuous density of states of the bulk solid to collapse into discrete electronic states (Figure 1.2).
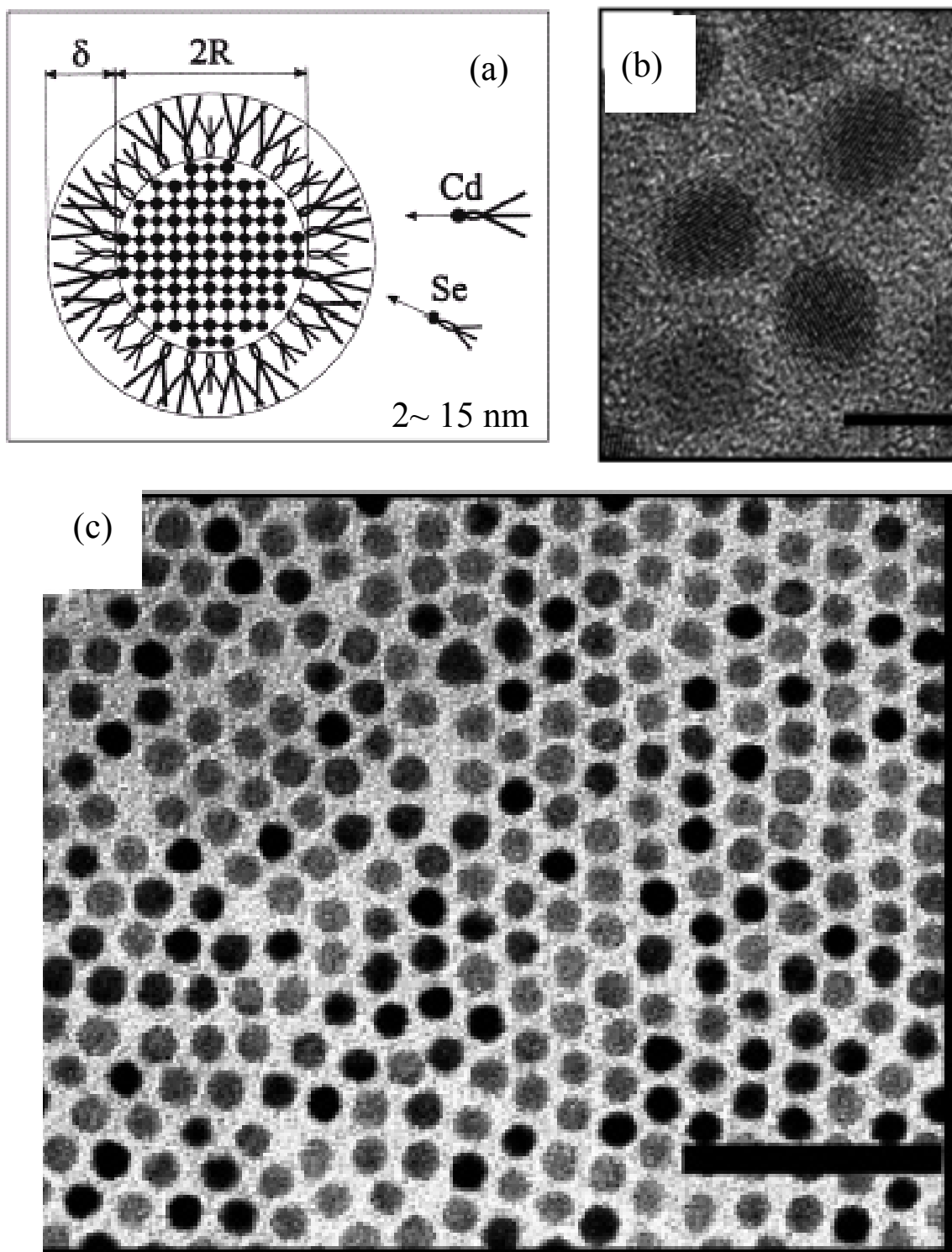
Figure 1.1 : Colloidal semiconductor NCs (a) Cartoon of NCs with a monolayer of organic molecule capping groups associated with the surface. (b) High resolutionTEM of a CdSe NCs, where actual atom columns can be seen. (c) A low resolution TEM of CdSe nanocrystals with hexagonally close packed.[1]

The unrestricted motion of carriers in bulk semiconductors is associated with a band structure with a density of states proportional to $E^{1/2}$ for each band. In quantum wells, motion of the carriers restricted to two dimensions leading to a constant density of states for each band. In quantum wires or rods, the carriers are confined in all but one dimension and the density of states begins to sharpen and NCs confine the carries in all three dimensions and atomic like states result.
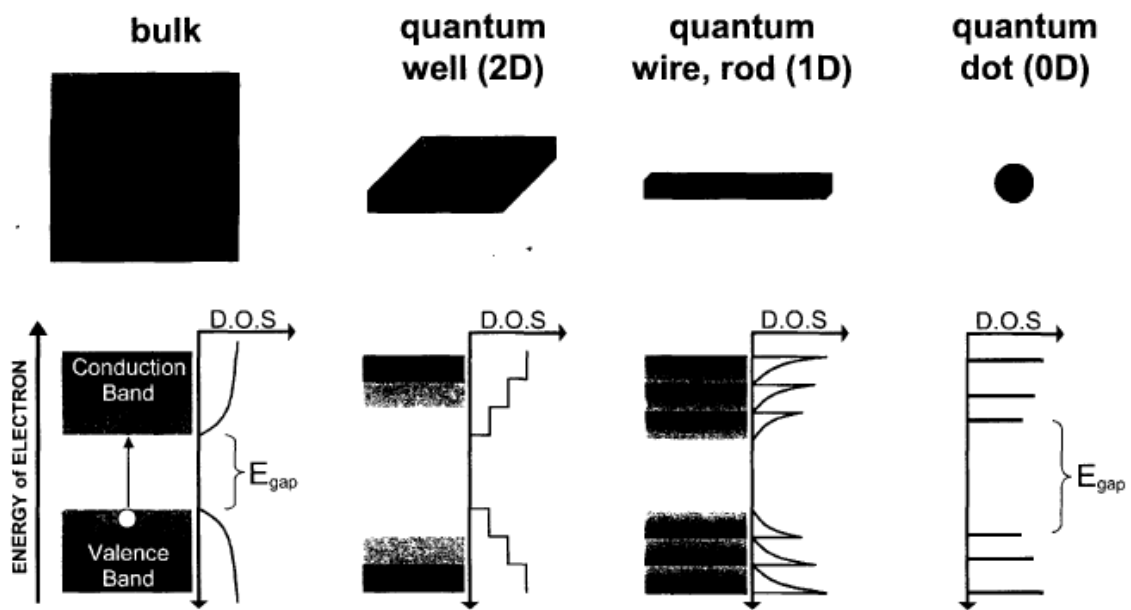
Figure 1.2 : Illustration of quantum confinement going from bulk semiconductor to quantum wells to wires or rods and finally to quantum confinement in all three dimensions in quantum dots or NCs. [2]

Semiconductor NCs are much like "artificial atoms" due to their quantized electron and hole states, which are very different compared to bulk materials that have energy bands. (Figure 1.3) This means that not only are the absorption and emission spectra of QDs blue-shifted from the bulk, but they also are no longer featureless. Both effects, blue-shifting as well as energy quantization, can be seen in Figure 1.4, The absorption spectrum of CdSe QDs with over 10 nm in diameter appears quite similar to that of bulk CdSe, being quite broad and featureless, as it experiences very little additional confinement from the bulk. Sharp transitions as well as a significant blue-shift are quite evident in the absorption spectra for the CdSe QDs with diameters smaller than 12 nm (the bulk exciton Bohr diameter).
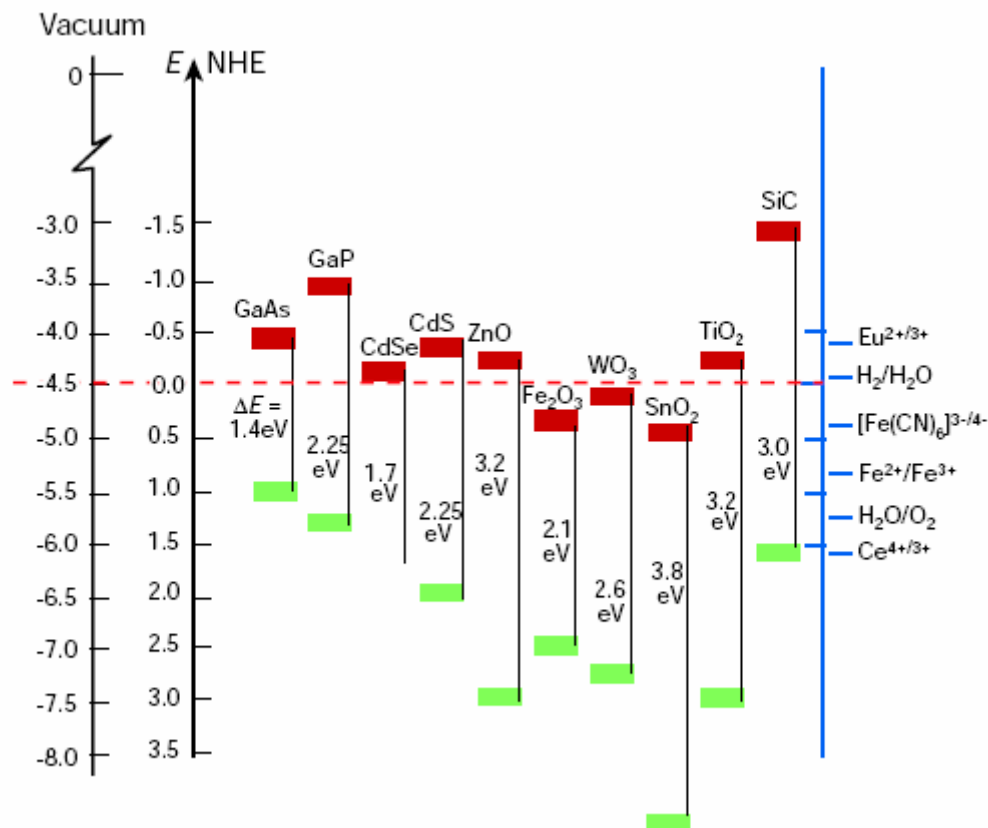

Figure 1.3 : The energy level of general II-VI semiconductor materials[3]

The emission properties of colloidal QDs are also quite unique, which have been observed spectroscopically for a series of QD samples as a blue shift in the absorption edge and band edge emission and a larger separation between electronic transitions with decreasing QD diameter[4] (Figure 1.4).
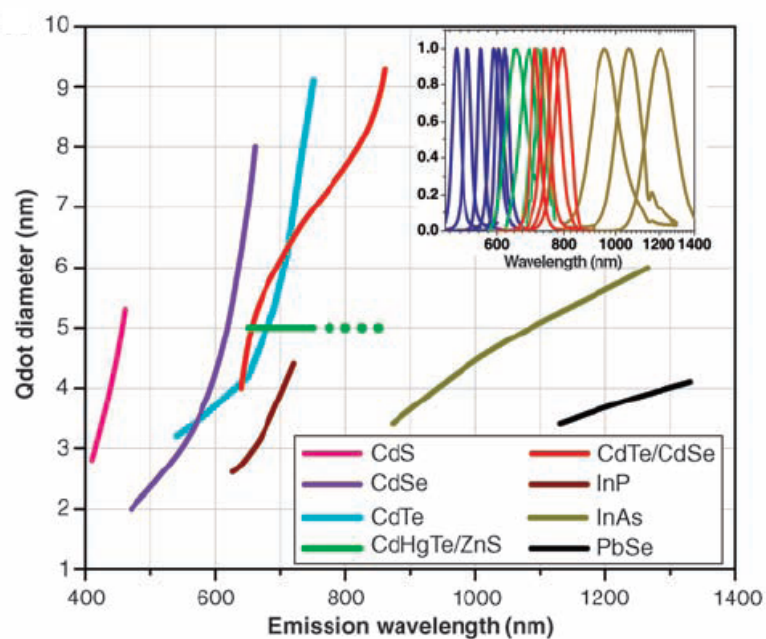

Figure 1.4 : Emission and sizes of QDs of different composition. QDs can be synthesized from various types of semiconductor materials (II-VI: CdS, CdSe, CdTeI; III-V: InP, InAs; IV-VI:PbSe) characterized by different bulk band gap energies. The curves represent experimental data from the literature on the dependence of peak emission wavelength on QD diameter. The range of emission wavelength is 400 to 1350 nm, with size varying from 2 to 9.5 nm. All spectra are typically around 30 to 50 nm (FWHM). Inset: Representative emission spectra for some materials.[5]

The absorption spectra shown in Figure 1.5(a) for ZnSe QDs and (b) for CdSe QDs, the emission color can be tuned based on the diameter synthesized shown in Figure 1.5 (c) as well. CdSe with a bulk band gap of 1.73 eV[5](i.e. 716 nm) can be fabricated to emit across the entire visible spectrum as seen in Figure 1.5(b), where CdSe QDs with 2 nm in diameter emit blue color and those with 8 nm emit in red color. The ability to tune the optical properties of QDs with size is presented.
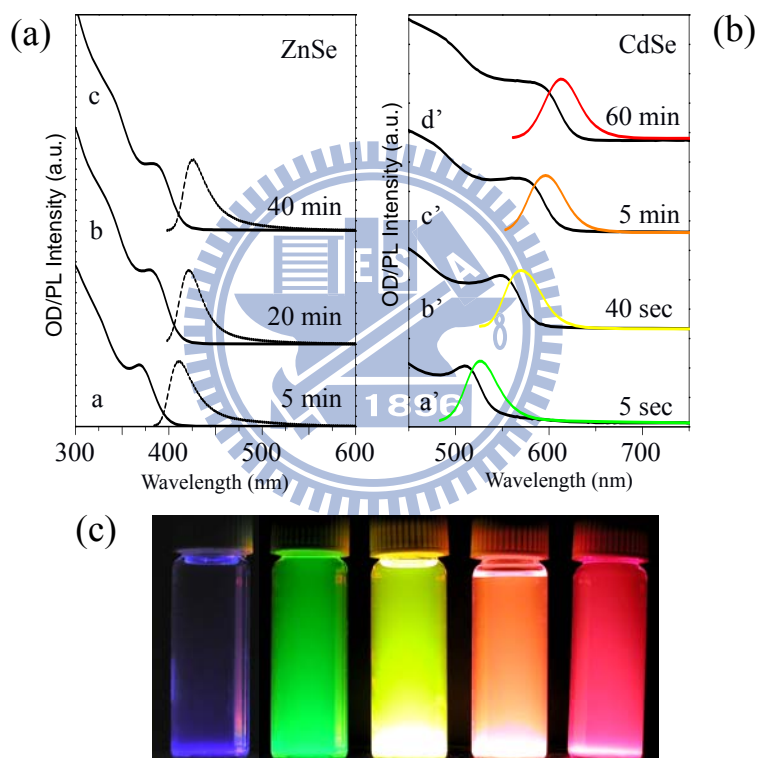

Figure 1.5 : Absorption spectra of a size series (a) ZnSe QDs and (b) CdSe QDs , demonstrating optical tunability of QD with size. (c) Vials containing different sized CdSe QDs (2 to 8 nm in diameter) dispersed in CHCl₃ solution showing fluorescing different color variation solely due to size difference.

Single CdSe QDs have been shown to exhibit ultra-narrow homogeneous linewidths of emission, but due to difference in size, shape, and local environment, the ensemble emission linewidth is significantly broadened[6]. Typical full width at half maximum (FWHM) of high-quality CdSe QDs is ~20 nm. As a result, the FWHM of the emission spectrum for a given material becomes a good indication for the size distribution of the sample. The absorption spectrum serves as a guide to the size distribution of a sample in the same manner. The more uniform in size and shape a QD sample is, the more features will be seen as well as the more distinct and sharp each feature will appear in the absorption spectrum.

As described, the excellent optical properties of QDs have been attended chunks of attention on different applications. Such as bioimaging material and optoelectronic devices, in particular, in the filed of devices, many groups have investigated into the chemical, physical and electrical properties when QDs are applied in various optoelectronic devices.

1.1.2 Organic Light Emitting Devices

The first vacuum-deposited organic light emitting device (OLED) fabricated from thin amorphous organic small molecule films with low operating voltages (< 20 V) was reported by Tang in 1987. This potential technology was quickly recognized. Shortly after this demonstration of vacuum deposited molecular materials, Burroughes et all synthesized polymeric materials and applied them into efficient electroluminescent devices[7]. The field of OLEDs was developed rapidly when it was expected to achieve the bright and efficient flat panel displays[8]. Much work has been reported in attempt to improve the external quantum efficiency (EQE)[9],[10] lowering operating voltages[11], increasing device lifetime[12] and narrowing their emission spectra[13]

One of the major advantages OLEDs have over traditional flat panel display technologies is based on the ability to deposit the organic materials over large areas in a more scalable manufacturing process making it potentially more cost effective. This is much more applicable to the polymer materials that can be inkjet printed than the small molecule organics that are typically deposited using vacuum thermal evaporation. Because the pixels in OLED displays are emissive and are either on or off, the contrast ratios are much better than liquid crystal displays (LCDs). The light in LCDs is generated by a white fluorescent backlight, which is then polarized and filtered to create red, green, and blue pixels. The liquid crystals function as a voltage driven light valve, allowing light to pass or not depending on the voltage

applied across the cell. When the crystals are oriented such that the polarized light is being

blocked, the pixel is off. The LCD pixels are, however, incapable of showing true black due

to some light always leaking through.

1.1.3 Historical Perspective of Hybrid LED

The device structure and operating principles of hybrid organic/inorganic quantum dot

light-emitting devices (QD-LEDs) and OLEDs are very similar. As a result, understanding

how OLEDs function is important to this body of work. The first small molecule OLEDs with

low operating voltages, made by Tang et all [14] were based on aluminum tris-

(8-hydroxyquinoline) (Alq$_3$) / N,N'-diphenyl-N,N'-bis(3-methylphenyl)- (1,1'-biphenyl)

-4,4'-diamine (TPD) single heterostructures, where Alq$_3$ served as both the electron transport

layer (ETL) and the luminescent layer (LL), while TPD functioned as the hole transport layer

(HTL). Figure 1.6(a) shows a cross-sectional diagram of a general double-heterojunction

OLED, where the functions of the ETL, HTL, and LL are performed by separate organic

materials. When a bias is applied across the Alq$_3$ - TPD single heterostructure, holes are

injected from the transparent anode (indiumtin oxide (ITO)) into the TPD and are transported

via hoping from one molecule to the next through the TPD to the TPD- Alq3 interface, where
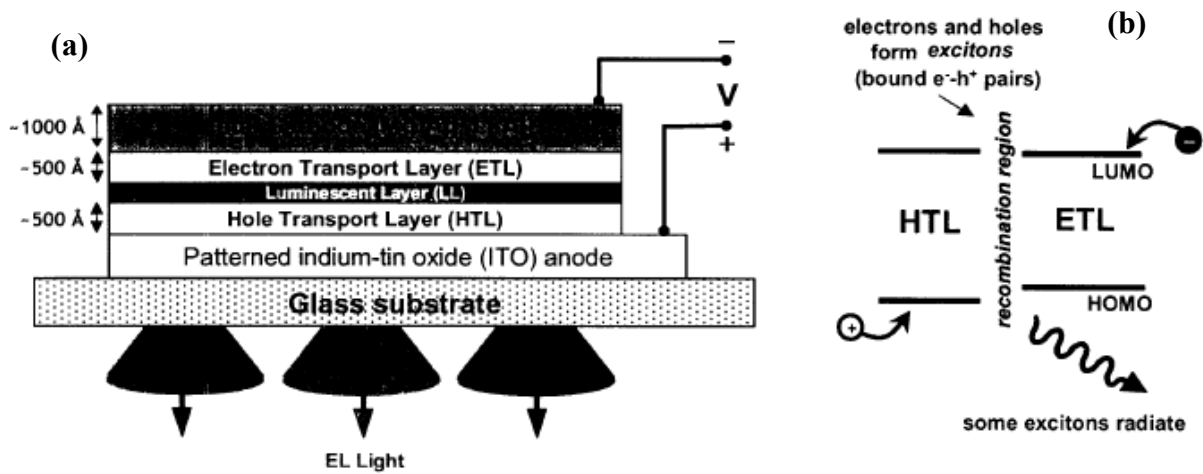
they buildup at the band edge mismatch (Figure 1.6(b))

Figure 1.6 : (a) The diagram of a general double-heterojunction OLED (b) Principle of operation of a typical OLED, where electrons and holes in their respective transport layers travel towards the recombination region created by the interface between the two films.

At the same time, electrons are injected from the low work function metal cathode into the Alq_3 and are transported via hoping through the Alq_3 thin film to the TPD- Alq_3 interface where they also accumulate. In the vicinity of the ETL-HTL interface, holes and electrons meet on TPD and Alq_3 molecules to form a tightly bound electron-hole pair (Frenkel exciton). The excitons live for approximately 1-10 ns (exciton lifetime), before they radiatively recombine generating light or nonradiatively recombine to generate heat. This region of the device where the excitons are generated and relax is known as the "recombination zone", whose width is determined by the diffusion length of carriers and excitons in the emitting material (Figure 1.6(b)). Excitons can diffuse from one molecule to another via energy

transfer processes before they relax and as a result all of the excitons in the TPD/Alq$_3$ device transfer their energy to the Alq3 molecules prior to relaxing. This is evident by the fact that no TPD emission is observed in these devices.

Injected electrons and holes are presumed to be uncorrelated in the process of electroluminescence (EL) and can form both singlet and triplet excitons. Approximately, one singlet exciton is created for every three triplet excitons in OLEDs[15] (based on their multiplicity) and because the ground state is typically spin-antisymmetric (like singlet excitons), only relaxations of singlet excitons conserve spin and generate fluorescence, while the energy in triplet excitons is wasted. Studies on Alq$_3$-based OLEDs indicate that 60 % of the carriers injected into the device do not form excitons, or form excitons that are rapidly quenched at defects or transfer their energy to surface plasmon modes in the metal electrode or to lossy waveguide modes[16]. Of the other 40 % of injected carriers that do form excitons that can contribute to a luminescent process, around 25 % are singlet states. When a luminescent guest molecule is embedded in a donor host material, the excited donor molecule (Donor*) can transfer its energy (exciton) to the luminescent acceptor molecule in the ground state (Acceptor). The two possible mechanisms for exciton energy transfer in OLEDs are Förster or Dexter energy transfer as shown pictorially in Figure 1.7.
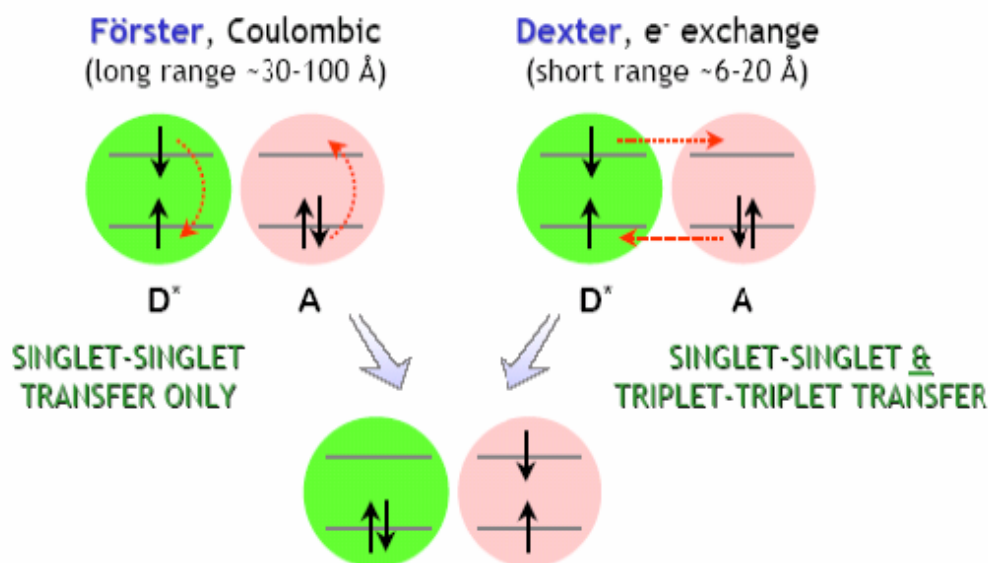
Figure 1.7: A representation of Förster and Dexter processes in energy transfer.

The luminescent guest molecules can also be directly excited (exciton formation directly on the guest molecules) if the energy level structure of the guest molecules relative to the host molecules causes electrons or holes to be trapped as the carriers are traveling through the host. In some doped organic thin films, exciton energy transfer can increase the luminescence of the guest molecules, while quenching that of the host molecules completely. Less than 1 % doping of guest molecules into the electrically pumped host layer is sufficient to quench the host luminescence. Low dopant concentrations provide highly efficient luminescence due to the reduction in exciton-exciton quenching when the guest molecules are separated from one another by relatively large distance

Looking back at the two major categories of devices fabricated prior to 2002, it is possible to analyze the shortcomings of these devices. For devices in which NCs were homogeneously distributed in a polymer matrix, the NCs were most likely strongly influencing the film morphology and charge conduction through the polymer layer. Rough surface morphology, typical of thick (more than a few monolayers) NC films likely contributed to the observed low device yields and allowed little freedom in optimizing charge injection, transport and position of the exciton recombination region. Both lumophores and charge transport layers. NC photoconductivity experiments provide direct evidence of the poor conduction properties of thick NC films relative to organic semiconductors[17]. Neat NC films are essentially insulating due to carriers having to overcome large energy barriers created by the organic capping molecules as they hop from one NC to the next (Figure 1.8(b)).

`   In addition, thin films that have both charge and excitons present often undergo quenching mechanisms such as polaron-exciton quenching or Auger recombination.[18] A single monolayer of NCs sandwiched between two thin films of molecular organic semiconductors allows the NCs to function exclusively as lumophores (Figure 1.8(a)). In small molecule OLEDs, charge injection transport and light emission are controlled using separate layers optimized for these functions.
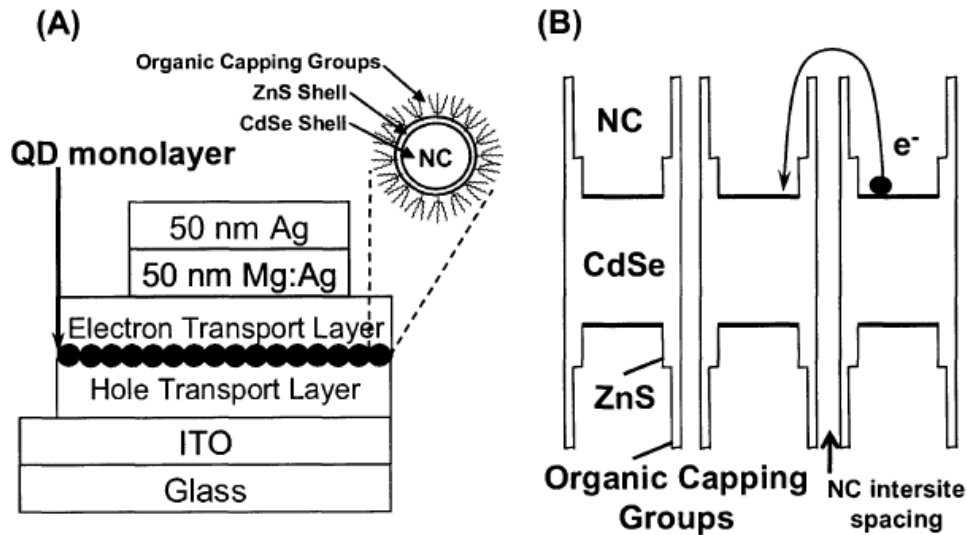
Figure 1.8 : (A) Basic QD-LED structure, where a monolayer of NCs is resides between a small organic molecule electron transport layer and a hole transport layer, which removes the need for the NCs to participate in charge transport while using them solely for their light emission properties. (B) Energy band diagram showing the difficulty of conducting electrons from one NC to another due to the large energy barrier created by the organic capping molecules on the NCs.[19]

1.2 Polymer Bulk Heterojunction Solar Cells

1.2.1 The Bulk Heterojunction Concept

There exists significant interest in organic/polymer bulk heterojunction (BHJ) solar cells due to their low temperature and solution processability. In addition, the important advantages of plastic solar cells include low cost of fabrication, ease of processing, mechanical flexibility and versatility of chemical structure from advances in organic chemistry. In order to obtain efficient photon-to-charge conversion, many different device architectures have been

developed, such as single-layer cells[20], doublelayer cells[21] and bulk-heterojunction-blend cells[22]. BHJ solar cells based on the intimate mixing of conjugated polymers and fullerene derivatives are mostly used. Because of the larger donor/acceptor (D/A) interface, which provides the exciton dissociation sites, a BHJ cell is more efficient than other bove-mentioned structures. A bulk heterojunction device is displayed schematically in Figure 1-9.
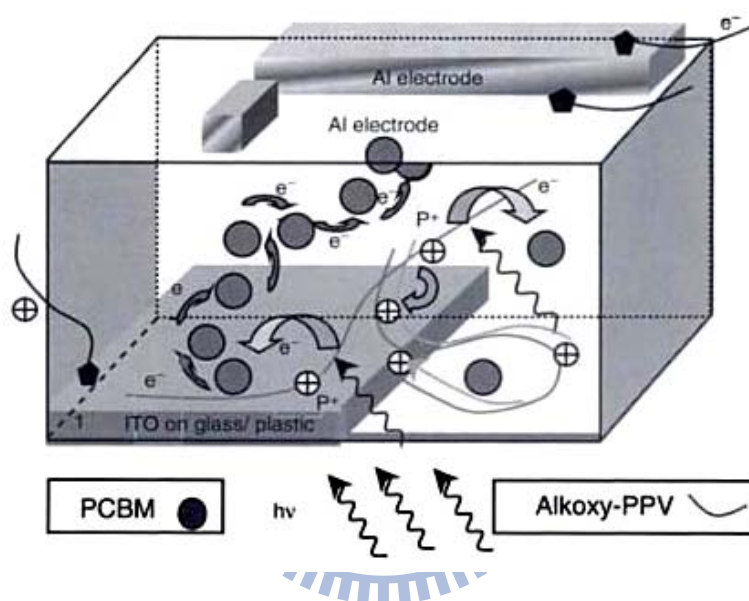

Figure 1.9 : Schematic description of bulk heterojunction solar cells.[23]

An overview of the chemical structures of organic materials presently used in different BHJ solar cells is given in Figure 1.10. Depending on which sorts of materials being used for the active layers, different separating layers are fabricated and reported.
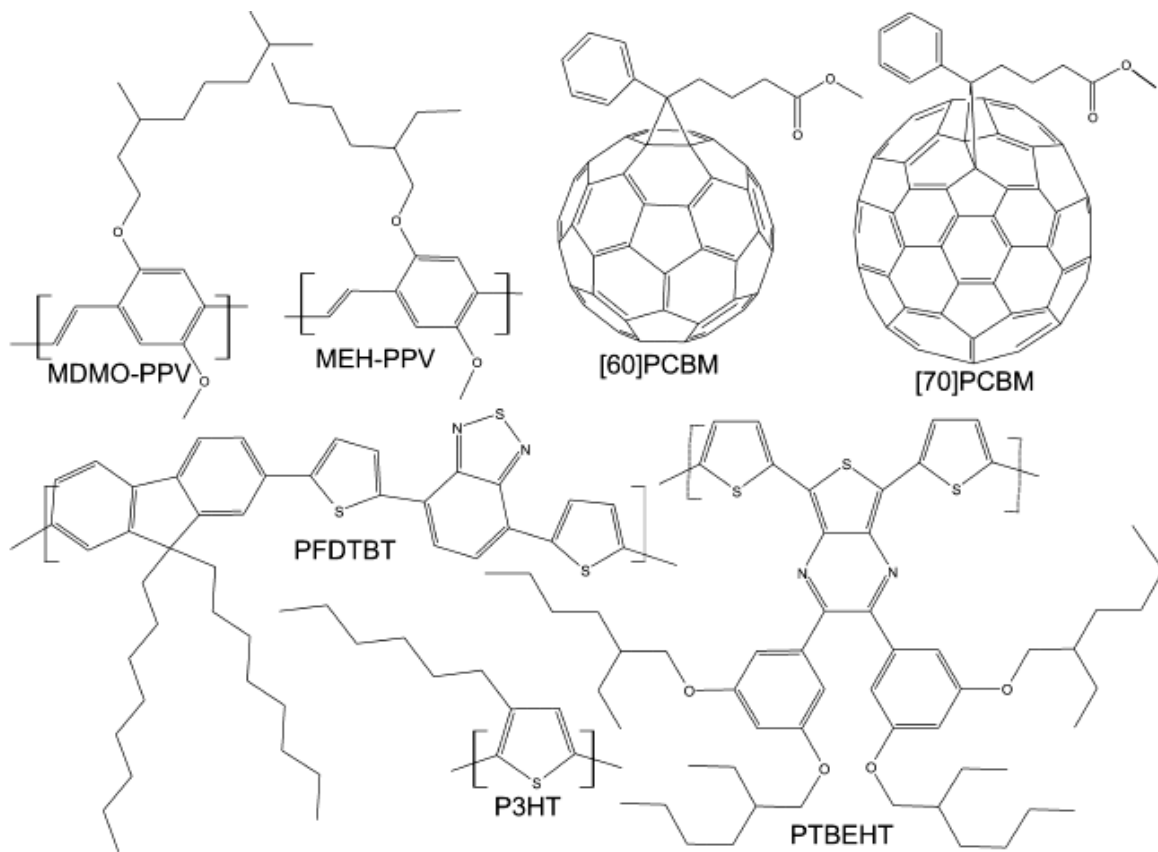
Figure 1.10 : Schematic description of photoactive materials.

1.2.2 Device Operation Principle

The bulk heterojunction devices used today consist, in general, of a PEDOT:PSS -covered ITO substrate coated with a single photoactive bulk heterojunction layer (e,g., polymer-fullerene mixtures) closed by a low work function aluminum cathode, as shown in Figure 1.11
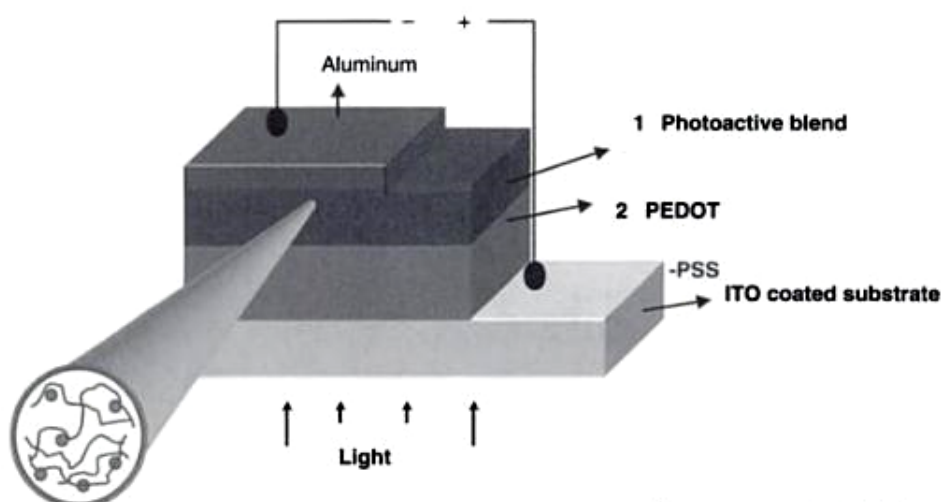
Figure 1.11 : Schematic description of device : ITO/PEDOT:PSS/polymer blend/Al

For polymer solar cells, the nature of the electrical contacts between the active organic layer and the electrodes is one of the most critical factors in determining device characteristics such as the short-circuit current density (J_{sc}), open-circuit voltage (V_{oc}), and the fill factor (FF). (Figure 1.12) Because the series resistance (R_s) in a solar cell is attributed to the bulk conductivity of each of the functional layers and the contact resistance between them, materials with high charge carrier mobility and Ohmic contact at the interfaces are required to obtain high J_{sc} values. Good matching of the Fermi levels of anode and cathode to the highest occupied molecular orbital (HOMO) of the donor and the lowest unoccupied molecular orbital (LUMO) of the acceptor, respectively, is also needed to maximize the V_{oc}. Another important parameter, the parallel resistance (R_p, or shunt resistance), is determined by the quality of the thin films and their interfaces. Small R_p values originate from the loss of charge

carriers through leakage paths including pinholes in the films and the recombination and

trapping of the carriers during their transit through the cell, leading to a decrease in device

performance.
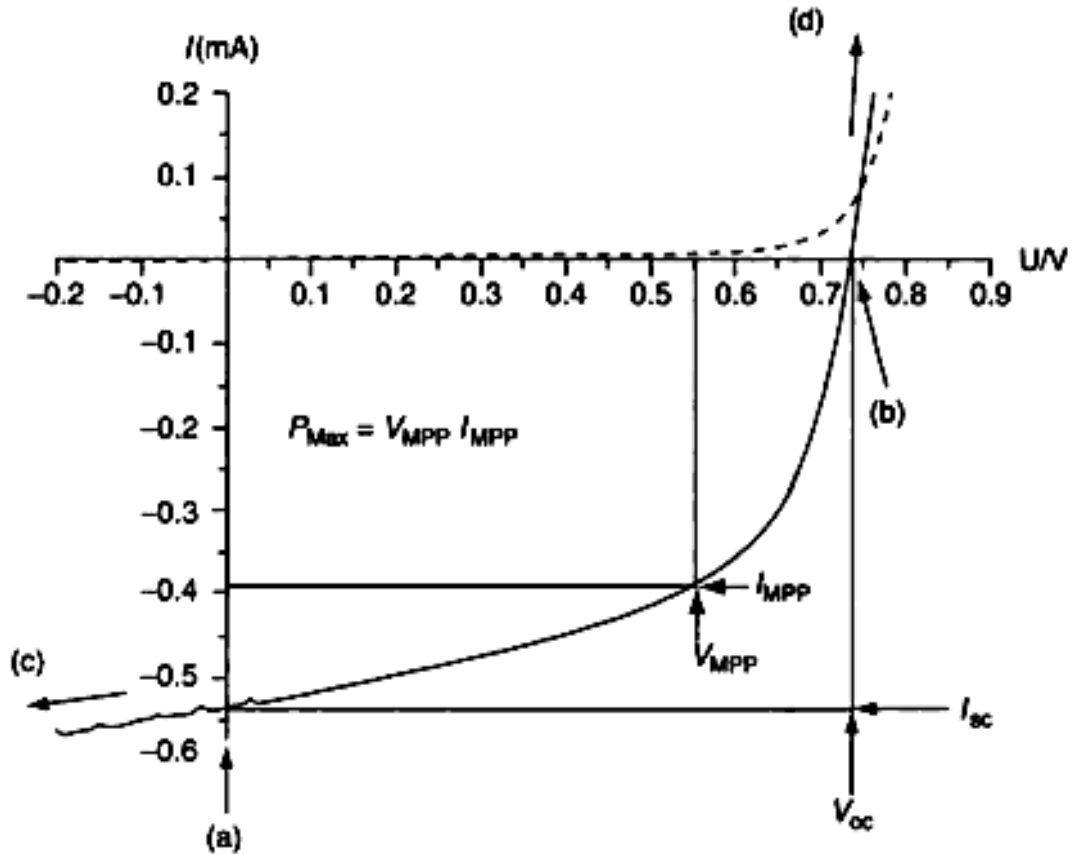
Figure 1.12: Current-voltage (I-V) curves of a MEH-PPV:C_{60} based solar cell (dark: dashed,

illuminated: solid line) The characteristic intersections with the ordinate and the abscissa are

the open circuit voltage (V_{oc}) and the short circuit current (I_{sc}). The largest power output (P_{max})

is determined by the point where product of voltage and current is maximized. Division of

P_{max} by the product of I_{sc} and V_{oc} yields the filling factor (FF).

1.3 Motivation

The first part of QD-LED is to create layered structures of distinct materials is one of the principals advantages of polymer OLEDs. PLEDs have the flexibility and diversity of polymer design as well as the low cost of wet deposition techniques which do not require the use of vacuum equipment, while PLEDs have the higher purity of available materials, the reproducibility and thickness control of vacuum evaporation, and ultimately the higher performance metrics that have been achieved. We have the advantage of being able to combine semiconductor NCs with both sets of deposition techniques and materials, thus can pursue the technology that seems more promising. All previous work attempting to create efficient QD-LEDs focused on using polymers as the NC matrix, in the following part, we incorporated NCs into polymer OLEDs by using two common methods. Thus, QD-LED devices that is both more efficient and easier to optimize.

The second part focuses on the design of ZnO-based Inverted single and tandem polymer solar cells. Since 2005, device with high efficiency (i.e. 4.4%) have been demonstrated the efficient polymer solar cells with power conversion efficiencies (PCE) in regioregular poly-(3- hexylthiophene) (RR-P3HT) and [6,6]-phenyl C_{60} butyric acid methyl ester (PCBM) blend[24,25].Recently, in 2008, PCE of regular polymer solar cells have reached over 5% through careful control of morphology and the use of low band gap materials.[26,27] However, for practical applications, the efficiency of polymer solar cells needs to be over

10%, and they have to have good environmental stability.[28] To achieve these goals, other issues such as optimization of electrical contact at different interfaces in the polymer solar cells[29] and the development of new device structures are equally important. In the chapter 5,6 sections, the different types of organic tandem and multi-junction photovoltaic cells are described and recent results obtained by various groups and our new design for single and tandem polymer solar cells will be presented

1.4 Thesis organization

The overview of organic Hybrid Organic/Inorganic Light Emitting Devices and Polymer Bulk Hetero-junction (BHJ) Solar Cells are reviewed in the beginning and the motivation of this dissertation is briefly introduced. This thesis is organized as follows.

➢ In Chapter 2, a brief introduction of the materials, experimental setup and equipments are described in detail.

➢ In Chapter 3 introduces the semiconductor CdSe/ZnS and discusses in detail the synthesis, characterization, and properties, as well as how the application CdSe/ZnS QDs into device. The fabrication and EL characterization of a white-emitting hybrid QD-LED by integrating core-shell CdSe/ZnS QDs acting as a yellow emitter and polyfluorenes as the blue emitter in a multilayered structure.

➢ Chapter 4 introduces the synthesis and characterization of the zinc oxide (ZnO)

materials, followed by the fabrication of the resulting ZnO based polymer solar cells. The design of a ZnO nano-ridge structured film that can be used as an electron collection layer in an inverted polymer solar cell. The ZnO nano-ridge structure was formed by a simple sol-gel process using a ramp annealing method.

➢ Chapter 5 discusses the study of a highly efficient tandem polymer solar cell with inverted polarity. The optically transparent interlayer, consisting of a molybdenum trioxide (MoO_3) layer and an amorphous ZnO, serves as the interconnecting layer facilitating charge recombination between the bottom and top sub-cells. The ZnO layer, prepared by a low temperature process, provides a dense layer for electron collection and a barrier against solvent from dissolving the under layer. The leads to the high photovoltaic performance in both single and tandem inverted solar cells.

➢ Chapter 6 consists of the conclusion and achievements of this thesis. Finally, strategies for further improvement are discussed, with outlooks for future research given.

Chapter 2

Experimental Methods

2.1 Materials

All the chemicals were purchased from Sigma Aldrich, Acros, Merck, Lancaster, TCI, Rieke Metals, and Frontier Carbon Corp. Indium tin oxide (ITO)-coated glass (15 Ω/cm^{-2}), the substrates were sequentially cleaned prior to use by ultrasonic agitation in a detergent solution, acetone, isopropanol, and distilled water.

2.2 Equipments

UV-Vis Spectrophotometer

Absorption spectra of QDs and polymers were measured with a Hitachi model U-3010 UV-Vis Spectrophotometer. The concentration of the CdSe samples for PL and UV-Visible measurements were 20 mg in 5ml chloroform.

Spectrofluorometer

Photoluminescence (PL) excitation and emission spectra were collected at room temperature using a Jabin-Yvon Spex Fluorolog-3 spectrofluorometer (Instruments S.A., N.J., U.S.A) equipped with a 450 W Xe light source and double excitation monochromators. The spectral response of the measurement system is calibrated automatically on start up. The emission spectra of various QDs were obtained using an excitation wavelength (λ_{ex}) of 367 nm.

Transmission Electron Microscope (TEM)

JEOL JEM-2010EX at 200 kV was used for morphology measurement.

Scanning Electron Microscope (SEM)

JSM 6400-F was used for the measurement of surface morphology, the amorphous ZnO-d is difficult to distinguish due to the poor contrast of the image of HR-TEM. Therefore, the SEM image at 100 kV is useful to observe the cross-sectional of device and the surface morphology

Atomic Force Microscope (AFM)

Film thickness was determined by using AFM and an Alpha-Step 500 surface profiler (KLA Tencor, Mountain View, CA, USA). AFM images show that the surface of a 5μm × 5μm or 500nm ×500nm surface area sample has a root-mean-square (r.m.s.) roughness, indicating the presence of an extremely smooth surface and fine phase separation.

I-V Measurements

Current-Voltage characteristics of the solar cells both under dark and light were taken using a Kiethley 4200 source unit. I-V measurement under light bias was taken under stimulated AM1.5G spectrum using an Oriel 9600 solar simulator.

External quantum efficiency (EQE) measurements

 (EQEs) were measured by using a lock-in amplifier (SR830, Stanford Research Systems)

under short circuit condition when the devices were illuminated by monochromatic light from a xenon lamp passing through a monochromator (SpectraPro-2150i, Acton Research Corporation). The measurement for the tandem cells and single cells were performed according to the method proposed by Kim et al.[30] Nevertheless, it should be noted that measurement using this method is appropriate for the case in which the two sub-cells have shunt resistance large enough such that photocurrent at a finite negative bias does not vary significantly from the short circuit point. Since the monocolor light bias induces strong absorption in one of the sub-cells, a finite photovoltage is developed across the sub-cell. This photovoltage induces a negative bias across the sub-cell whose EQE is being measured. Therefore, if the photocurrent varies significantly, when the other sub-cell is still in off state, the carriers are blocked within the inter-connection layer as we discuss later, imposing a considerable bias voltage onto the other sub-cell. Therefore the EQE of the sub-cell that is taken under short circuit condition of tandem cell is in reality taken under reverse bias condition of the sub-cell. This leads to overestimation of EQE value if the photocurrent is sensitive to the applied bias. This makes evaluation of EQE of tandem cells complicated, and extra care has to be taken.

Chapter 3

Hybrid White-Light Emitting QD-LED

3.1 Background and Motivation

The roles of either nanocrystals or nanopartilces integrated in PLED are classified into two functions. The first one act as a mixer to enhance the device performance and the other one acts as an emitter.

3.1.1 Blending Method

Utilization of the nanocomposites to enhance the performance of PLEDs was proposed several years ago from 1995. Several studies have been carried out to enhance the current density, radiances, and power efficiency properties by mixing oxide nanoparticles (TiO_2, SiO_2) into electroluminescent polymer materials like MEH-PPV [31]. Moreover, photovoltaic efficiency of PPV derivatives could be improved by the incorporation of C_{60} nanoparticles[32]. Kim et al. reported the method of blending small amount of 5 nm gold nanoparticles into polyfluorene(PF) or PPV, resulting in an enhancement in quantum efficiency and oxidation stability[33]. To date, Lee et al. reported results on investigation of bilayer light emitting diodes made of organic capped CdSe(ZnS) core/shell type nanocrystals and poly[2-phenyl-3-(9,9-dihexyl-fluoren-2-yl) phenylene vinylene]- co- [2-me thoxy-5-(2_-ethylhexyloxy) phenylene vinylene] (FP-PPV-co-MEHPPV) electroluminescent co-polymer. Device structure: ITO/PEDOT:PSS/FP-PPV-co-MEH-PPV/Ca/Al devices have

been fabricated and studied. The co-polymer device emits a yellow light with a maximum

brightness of 3949 cd/m^2 and a maximum external quantum efficiency of 0.27 cd/A at 10V.

Incorporation of CdSe(ZnS) quantum dots into the active polymer film resulted in an increase

in device brightness, which reached 8192 cd/m^2 and in external quantum efficiency, which

became 1.27 cd/A at 7V with a lower turn-on voltage. The results indicate that CdSe(ZnS)

quantum dots improved significantly the emission of the devices by modifying the injection

and transport of the charge carriers. We suggest a non-uniform dispersion of QDs in the

co-polymer layer with carrier blocking process by the particles, which produced a balanced

charge distribution inside the co-polymer, and thus increased the emission efficiency shown
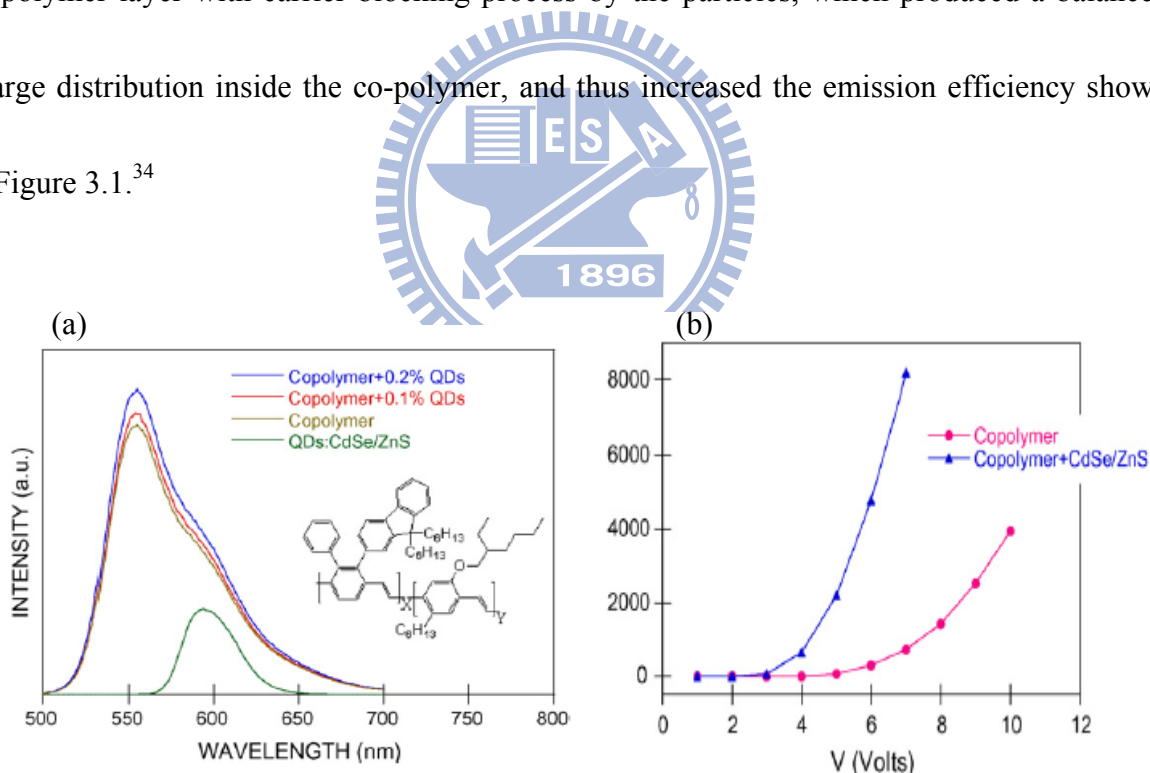
in Figure 3.1.[34]

Figure 3.1 : (a) PL spectra of pure co-polymer, co-polymer/QDs thin films and QDs in

solution. Inset shows the chemical structure of the co-polymer. (b) Luminance–voltage

characteristic of device with or without QDs at T = 300 K.

3.1.2 Bonding Method

Chou et al. reported that with the incorporation of surface-modified CdS nanoparticles into dendron-substituted polyfluorene, the luminescence of CdS NP could be enhanced by as much as three times [35]. Yang et al reported the synthesis of sulfide-containing poly(1,4-phenylene vinylene) derivatives, and these polymers have the advantage of permitting the coordinate bonding of sulfur atoms with CdSe through ligand exchange process[36]. By incorporating CdSe QDs onto sulfide-containing conjugated polymer S-PPV, the device performance was significantly improved as compared to the pristine polymers. Moreover, Yang et al demonstrated the synthesis and characterization of series of fluorene-based copolymers with pendent sulfide groups attached on the C-9 positions of the fluorene unit. The CdSe was grafted to the sulfur atoms by the ligand exchange reaction. FTIR spectra display two new peaks at around 1000 ~ 1100 cm^{-1}, indicating new force formation between sulfur from polyfluorene copolymers (PF1) (comprised of 9,9-dihexylfluorene,9,9-di[11-(decylsulfanyl)undecyl]fluorene, triphenylamine or benzo-thiadiazole moieties were synthesized by palladium-catalyzed Suzuki coupling reaction.) and CdSe (Figure 3.2a) As CdSe QDs were incorporated onto polymers via chemical bonding, the device performance was significantly increased as compared to their pristine polymers. The electrical characteristics of the diodes reveals that QDs can effectively increase the luminance and reduce the current density of devices. Hole-only and electron-only devices

fabricated from these nanocomposites demonstrate that CdSe QDs exactly block the hole and

trap the electron in the light-emitting layer, respectively. Consequently, the

electroluminescent efficiency of the light-emitting materials was effectively improved. The

present chemical bonding process of NCs and conjugated polymers could offer a general
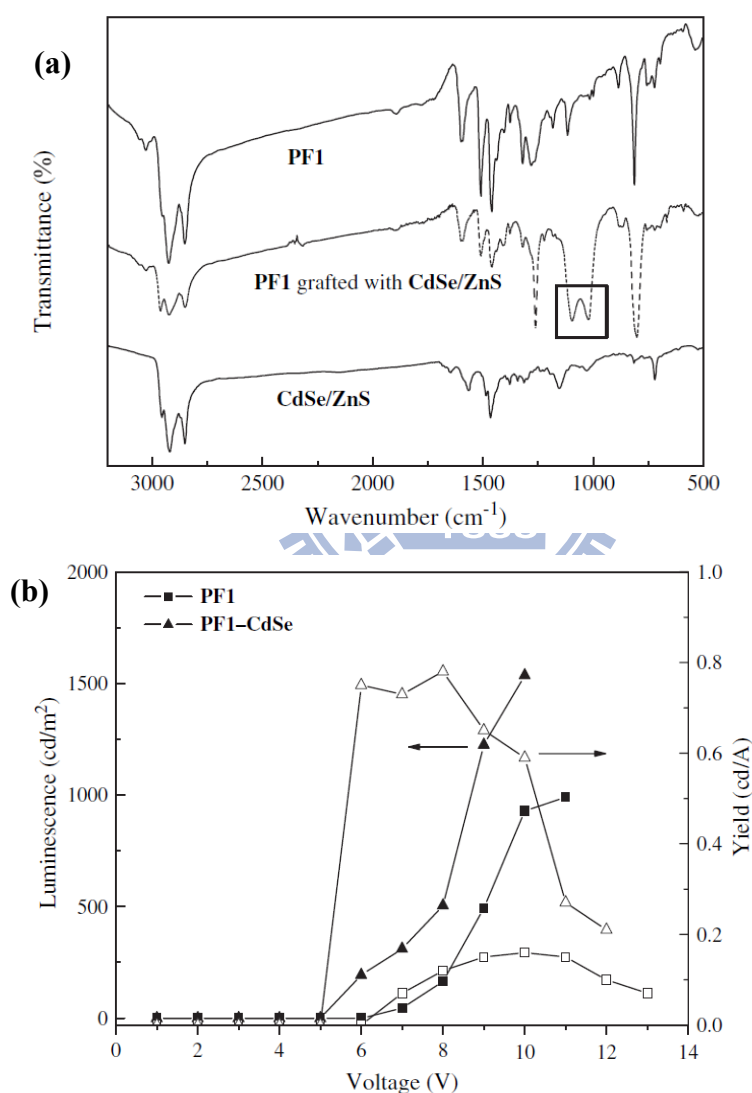
strategy for fabricating high-performance QD-LED.[37]

Figure 3.2: (a) FT-IR spectra of PF1, PF1-CdSe/ZnS nanocomposite and CdSe/ZnS. (b)

Luminescence-voltage efficiency characteristics of the PF1 and nanocomposite LED devices.

3.1.3 Layer-By Layer

In the devices where NCs were deposited as thick, neat films, the NCs functioned as a emitting layer. The hybrid optoelectronic structures usually consist of multilayer structures. Rough surface morphology, typical of thick (more than a few monolayers) NC films likely allowed little freedom in optimizing charge injection, transport and position of the exciton recombination region. Park et al reported the strategics of fabricating white-emitting QD-LEDs by blending CdSe NCs with varied particle sizes for different and complementary color purities into blue-emitting PPV-polyfluorene copolymers to generate white light[38]. Our research first reported on the hybrid white light emitting device based on polyfluorenes-based polymer with different functional groups and monochromatically emissive QDs. In this work, we report the fabrication and characterizations of a hybrid white light-emitting LED essentially based on a bilayer structure formed by blue-emitting polyfluorene derivatives and yellow-emitting QDs. Moreover, two types of blue-emitting polymers having different functional groups, poly (9,9-dioctylfluorenyl-2,7-diyl) – end capped with DMP (PFO) and the PF1 By tuning the thickness of QDs layers.

Here we have investigated the characteristics and EL performance of the hybrid white-emitting OLED device with bilayered structure of blue-emitting polymer and yellow-emitting QDs.

3.2 Device Structure Design and Experimental Details

The schematic device structure (Figures 3.3(a) and the chemical structures of the two blue-emitting fluorene derived polymers, PFO and PF1, used in this research are represented in Figures 3. 3(b) and 3.3(c), respectively. Essentially, PFO is a decent blue emitter and has a backbone resembling that of a fluorene molecule, except both ends capped with dimethylphenyl (DMP) group. On the other hand, in attempt to investigate the effect of interaction between polyfluorene molecule and QDs on the performance of the white-emitting EL device, we have synthesized a new blue-emitting PF1 containing H_3C-(C_7H_{14})-S-$(CH_2)_{11}$- functional group whose chemical structure is shown in Figure 3.3(c).
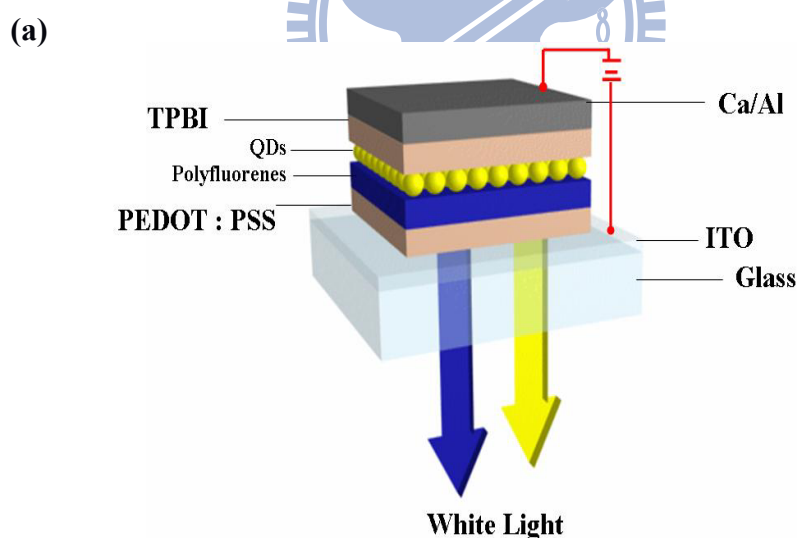
(a)

Figure 3.3 : (a) The schematic of the device structure   the chemical structures for polyfluorene derivatives
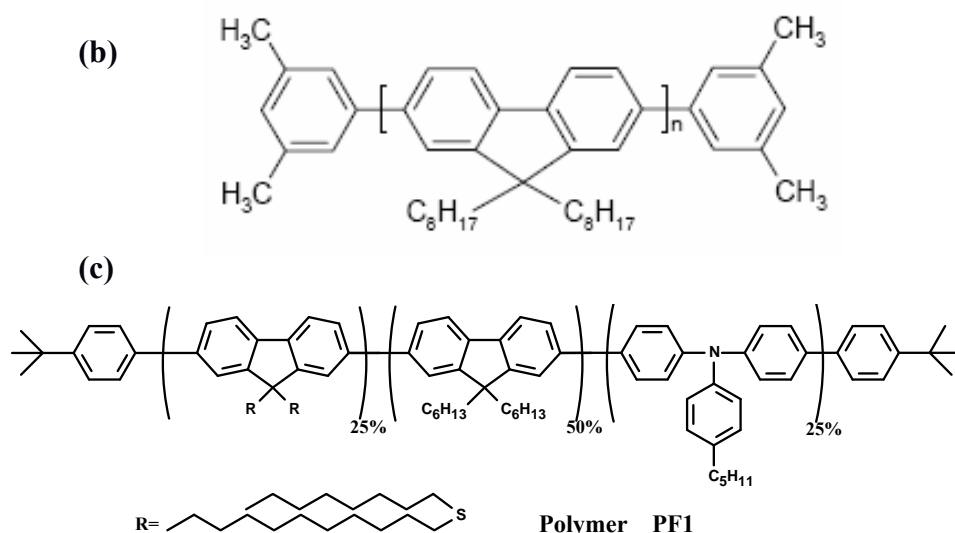
(b)

(c)

Figure 3.3 : The schematic of the chemical structures for polyfluorene derivatives (b) PFO and (c) PF1

CdSe NCs were prepared by a modified high temperature synthesis proposed by Reiss et al. with minor modifications[39],[40]. All manipulations were performed using standard anaerobic techniques. In a typical synthesis, a selenium stock solution was prepared in a dry box under a nitrogen atmosphere. As soon as the formation of a CdO/trioctylphosphine oxide (TOPO)/ hexadecylamine (HDA) complex at 330°C, the color of the solution turned from reddish to colorless. The system was cooled to 270°C, and the selenium stock solution was swiftly injected into the reaction vessel in a single step. Further growth occurred at 230-270°C depending on the desirable size of CdSe QDs. To prepare CdSe nanocrystals with sizes above 3.0-7.0 nm, additional injections of stock solution were required. The ZnS shell on the top of CdSe core was grown by a slow addition of dimethylzinc/sulfide stock solution to the solution of CdSe cores in the TOPO/HDA mixture at 180–220°C. The thickness of the ZnS shell is

about 2~3 monolayers. The obtained CdSe/ZnS samples were washed twice by dissolution in

chloroform and subsequent precipitation with MeOH. The quantum yield of the CdSe/ZnS

nanoparticles in hexane used in these measurements was ~ 50%. The bilayer films were

fabricated as sandwich structures between cathode (Ca:Al) and indium-tin oxide (ITO) coated

glass anodes. Approximately, 50 nm thick hole injection layer of poly-

(ethylenedioxythiophene) doped with poly (styrenesulfonate) (PEDOT:PSS) was spin-coated

on the top of ITO from a 0.7% dispersion in water and dried at 150℃ for 1 hr under vacuum.

Two polyfluorene-derived polymers (i.e., PF1: sulfur-containing polyfluorenes and PFO:

Poly(9,9-dioctylfluorenyl-2,7-diyl) – end capped with DMP) was spin-deposited from a

toluene solution onto the glass/ITO substrate. The coating thickness of PEDOT and polymers

together were about 100 nm, and the active areas were 0.04 cm^2. A layer of CdSe/ZnS QDs

with an average diameter of 3.8 nm was spin-coated from a hexane solution with an optical

density (OD) of 1.0 and 3.0 at the first nanoparticle excitonic absorption maximum, with the

different concentrations solution being found to produce thicker and thinner layer of QDs

when spin-coating was performed at 2000 rpm (this speed was used for all devices).

Subsequently, 30 nm thick of 1,3,5-tris (2-N-phenylbenzimidazolyl) benzene (TPBI) as a

electron transporting layer, and layered electrode materials of Ca (35 nm thick) and Al (100

nm thick) were thermally evaporated onto the QD layer as the cathode material at background

pressure lower than 2×10^{-6} Torr.

3.3 Results and Discussions

The UV-Vis absorption and PL spectra of the CdSe QDs in chloroform are shown in Figure 3.4(a). By tunning the reaction time during synthesis, the QDs with varied diameters and different luminescent wavelengths can be synthesized. The QDs with ~3.8 nm in size (as indicated in the TEM shown in Figure 3.4(b) were adopted as the yellow-emitting material to obtain white emission by combination with blue-emitting polyfluorenes.
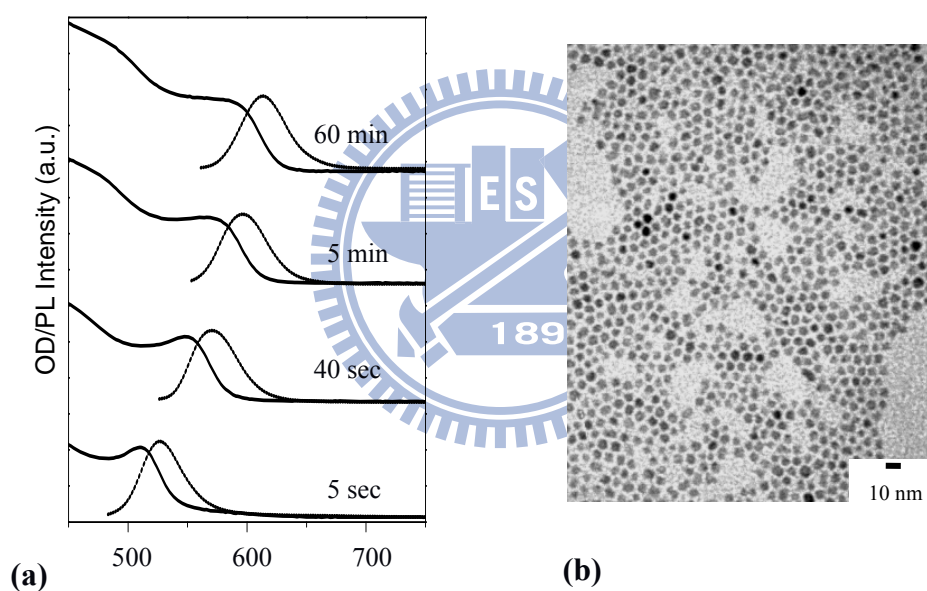

(a) **(b)**

Figure 3.4 : (a) UV-Vis absorption and solution PL spectra of CdSe QDs with the time scale counted from the addition of Se stock solution in synthesis. (b) TEM micrograph of CdSe nanocrystals with size of ~3.8 nm.
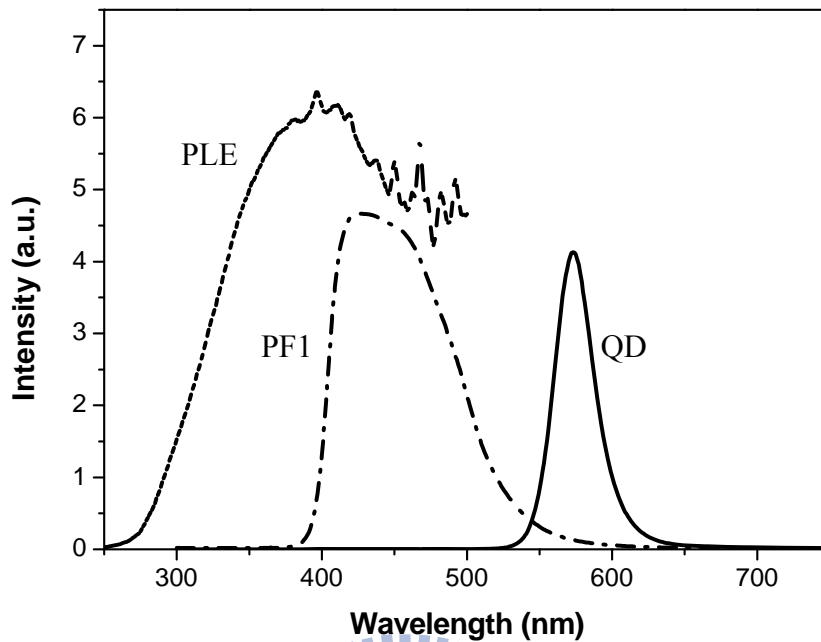
Figure 3.5 : PL (solid lines) and PLE (dotted) spectra of CdSe/ZnS QDs in hexane and PL spectrum of PF1 (dashed doted), showing the overlap between PL of PF1 and PLE of CdSe/ZnS QDs.

Figure 3.5 shows the PLE (dotted line) and PL spectra of CdSe/ZnS QDs (solid lines) and the PF1 (dashed doted line). We have observed that the emission of the PF1 as a donor and the excitation of the QD as an acceptor spectrally overlap with each other, which is required by Förster type energy transfer. Therefore, in our device described herein, energy transfer from the PF1 to QDs is expected when the polymer molecules and the CdSe/ZnS nanoparticles are within the Förster radius[41] in the bilayer type structure.
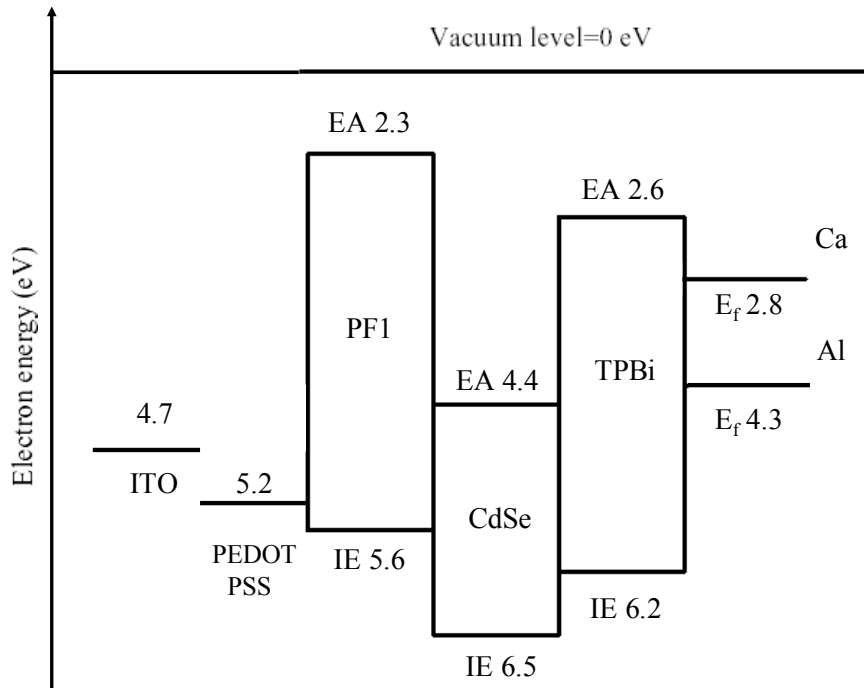
Figure 3.6 : Energy level diagram of the hybrid multilayered white-emitting QD-LEDs.

Figure 3.6 exhibits the HOMO-LUMO energy level diagram of the white-emitting

hybrid multilayered LEDs containing a bilayered CdSe QD/polyfluorene structure. The work

function of ITO, PEDOT:PSS and Ca/Al cathode, and the electron affinity (EA) and the

ionization energy (IE) of the PF1, electron transporting TPBI, and CdSe QDs are taken from

the experimental data reported previously[3]. Shown in Figure 3.7 is the applied voltage

dependence of EL spectra for the LED with the device structure of ITO/PEDOT/PF1/QDs (40

nm)/TBPI/Ca:Al. The intensity of EL spectra was found to be voltage dependent and increase

as the corresponding applied voltages increases from 13 to 17 V (from bottom to top) and

current density increases from 8 to 51 mA/cm^2. All spectra shown in Figure 3.7(a) have been

scaled to be on equal intensity for the emission peak of the QD emission (~578 nm). Similar

to that observed in the reported PPV/QD system, the observed broadened bandwidth of EL

peak was referred to an effect of both environment broadening (being in the solid state) and

local heating of the sample under large operation current flux[42]. Furthermore, we have also

observed in Figure 3.7(b) that EL luminescence at 578 nm measured on the

ITO/PEDOT/PF1/QDs (40 nm)/TBPi/Ca:Al devices was found to red shift for ~5 nm as

compared to that (i.e., 573 nm) of solution PL for CdSe QDs at ambient temperature. This

observation can be attributed primarily to an effect of reabsorption of the larger QDs within

the QDs layers due to an energy transfer from relatively smaller to larger QDs, or to the poor

thermal conductivity.[43]
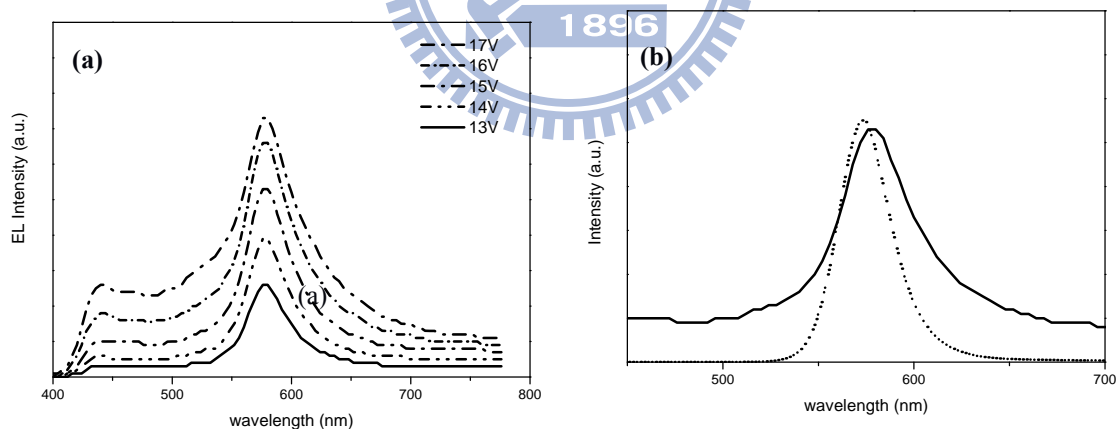

Figure 3.7 : (a) Applied voltage dependence of EL spectra for devices with ITO/PEDOT/PF1/QDs (40 nm)/TBPI/Ca:Al structure. (b) Comparison of band width of EL spectra (soild lines) at 13 V and that of solution PL spectra for QDs (dashed).

There are many characteristics in common between our hybrid QD/polymer LEDs and other reported organic material-based mutillayered LEDs devices.[44,45] For instance, the dependence of the EL intensity on QDs layers thickness and on applied voltage of our hybrid device is similar to those observed in PPV devices reported by other research groups[46] In our QD/ polyfluorenes- based devices, recombination of electrons and holes occurs either in the QDs layers or in the interface region between polyfluorene and QDs layers, which resulted in increasing EL intensity for the devices fabricated with QDs layers with thickness of 40 nm and show relatively stronger EL intensity with increasing applied voltages. The white-emitting hybrid QD-LED devices containing thinner QDs layer thickness (i.e., 10 nm) are expected and actually show improvement on the electron injection from the QDs layers into the PF1 layer. This will result in lower EL intensity of QDs than for devices with thicker QDs layer. Therefore, the combination of a limited electron range and electric field redistribution would be consistent with the observed EL dependence on the thickness of the QD layer. The observed voltage dependence of emissive color of QDs layer thickness may be correlated to either the electron range in the QDs layers or the electron injection rate from the QDs layer into the PF1 (for an electron at the heterojunction) layer, as rationalized and reported by Schlamp et al. in a fairly similar EL device containing emitting bilayers of CdSe/CdS nanocrystals/PPV[47].

The typical current-voltage (I-V) curves for the multilayered device with PF1/TOPO-HDA-capped CdSe/ZnS QDs bilayer. For comparison, the I-V curve of PF1/QDs-based device was substantially reduced and offset as compared to that for PF1-based device. This observation indicates that the presence of QD layer tends to reduce the charge mobility, which may be attributed to the trapping of injected holes or electrons by the yellow-emitting QDs layer and resulted in QD emission in the multilayer LED device. The corresponding EL spectra were shown in the inset of Figure 3.8. The EL band appearing at 480 nm is attributed to the recombination in the PF1 while the larger peak at ~573 nm was predominantly from the electroluminescence from the QDs layers. Based on the EL spectra, the 1931 Commission International de I'Eclairage (CIE) chromaticity coordinates for the hybird white-emitting device was determined to be (0.32, 0.37) at bias voltages below 9 V.
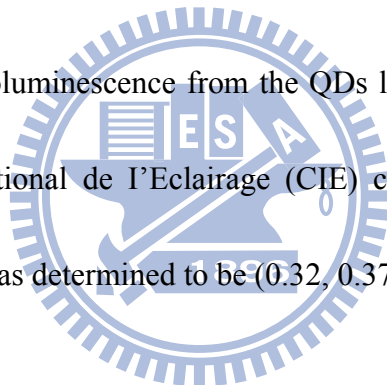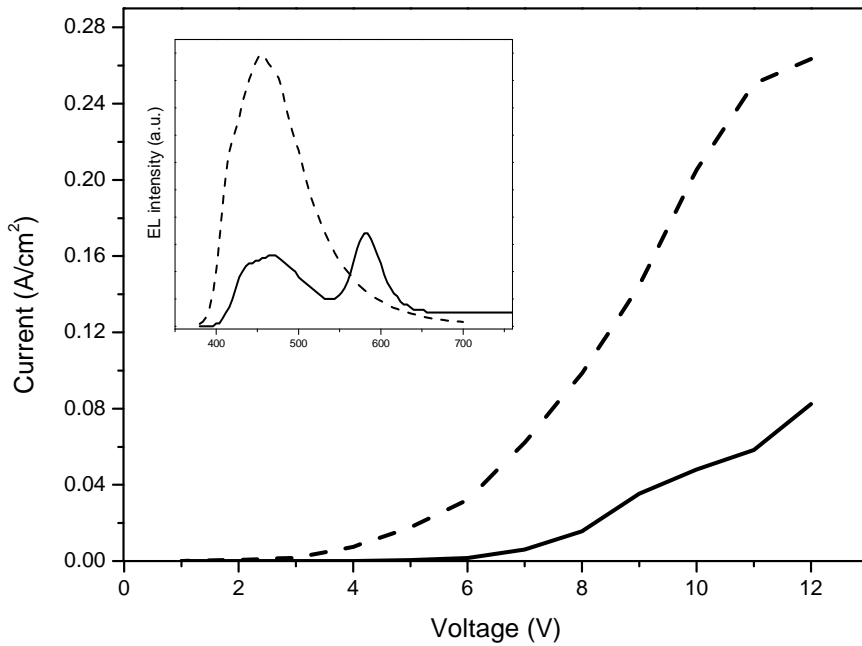
Figure 3.8 : I-V curves of the hybrid PF1/QD LEDs (solid lines) and PF1 LEDs(dashed). The EL spectra of the PF1 and PF1/QD LEDs are shown as a function of the bias in the inset. The bias voltages for the EL in the inset are 9.0 V (solid lines) and 6.0 (dashed).
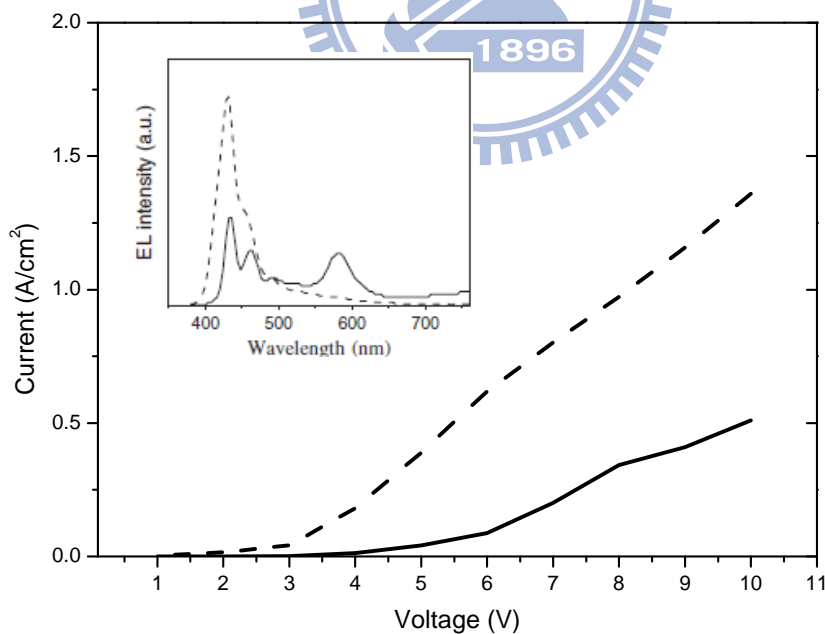

Figure 3.9: I-V curves of hybrid PFO/QD (solid lines) and PFO (dashed) LEDs. The EL spectra of the pure PFO and PFO/QD LEDs are shown as a function of the bias in the inset. The bias volatges for the EL spectra in the inset are 6.0V for both EL devices.

Figure 3.9 displays the EL spectra and the current-voltage (I-V) curves of the devices

with and without the addition of QDs, respectively. The trend is similar to that observed for

the PF1/QDs based devices represented in Figure 3.8, however, the offset of I-V curve for

PFO/QDs based device was found to be smaller than that observed in the PF1/QDs device. It

can probably be rationalized by considering the fluctuations in the film quality, the thickness

of QD layer or the extent of QDs surface coverage on top of the sulfur-containing

polyfluorene copolymers. The threshold driving voltage for PFO/QD device was found to be

smaller than that for PF1/QD systems. The EL spectra measured at 6 V of both the devices

with and without QDs addition are shown in the upper left inset of Fig. 3.9. Based on the EL

spectra, the 1931CIE chromaticity coordinates for the white light PFO/QDs based device was

determined to be (0.33, 0.33), which is close to that for the ideal white light.

3.4 Summary and Conclusions

In summary, the fabrication and characterizations of hybrid organic–inorganic white-

emitting EL devices, prepared from polymer/quantum dot nanocomposites comprising two

kinds of blue-emitting polymer, PFO and PF1, and CdSe/ZnS NCs. By tuning the thickness of

QDs emitting layers, we can control the easiness of electron injection from the yellow-

emitting QDs layers into the blue-emitting PF1 or PFO layer to generate white emission. Our

research results demonstrate that the simple spin coating method can be employed to obtain

white-emitting QD-LEDs with color chromaticity close to that of pure white.

Chapter 4

ZnO nano-ridge structure and its application

in inverted polymer solar cell

4.1 Background and Motivation

As mentioned in the previous chapter1-2, the power conversion efficiency (PCE) of regular polymer solar cell have reached over 4%, however, the further improvement in efficiency and stability is required. The regular device structure for polymer solar cells is indium tin oxide ITO/PEDOT:PSS/polymer blend/Ca/Al, where a p-type PEDOT:PSS layer is used for anode contact, and a low- work-function metal as the cathode. Both the PEDOT:PSS layer and the low-work-function metal cathode are known to degrade the device lifetime.[48] The PEDOT:PSS layer is potentially detrimental to the polymer active layer due to its acidic nature, which etches the ITO and causes interface instability through indium diffusion into the polymer active layer. Low work- function metals, such as calcium (Ca) and lithium (Li), are easily oxidized, increasing the series resistance at the metal/BHJ interface and degrading device performance. Therefore, highly efficient polymer solar cells using an inverted structure, in which the positions of the anode and cathode are reversed, have been demonstrated.[49,50] The low work function metal, e.g. Ca, used as the cathode in the regular structure, is replaced by a relatively non-reactive electron collection layer. This significantly improves the air stability of the solar cells.

Furthermore, vertical phase separation in polymer blends has proven to be advantageous in the inverted structure[51]. One important key to high performance inverted polymer solar cell is the selection of the electron collection layer.
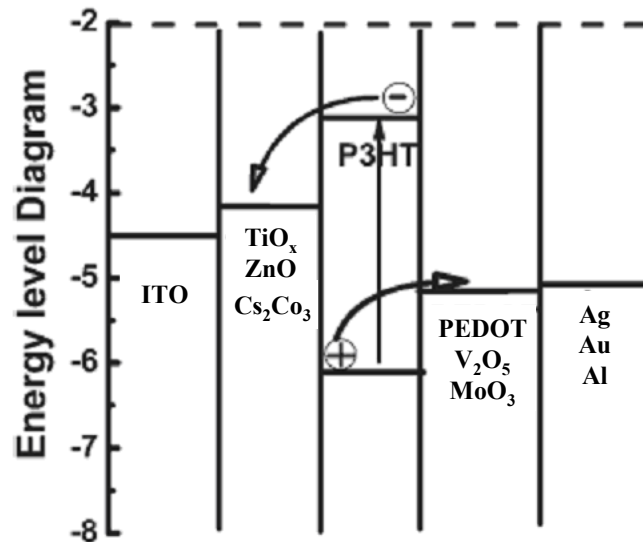

Figure 4.1 : The energy levels and different materials for inverted polymer solar cell.

The purpose of the electron collection layer is to provide hole blocking capability and a low resistive pathway for efficient electron extraction. Cs_2CO_3 have been demonstrated to be effective electron collection material[52,53] and the successful control on the work function can be modified from 3.45 to 3.06 eV by a low temperature (below 200 °C) annealing treatment. As illustrated in Figure 4.1, the direction of the dipole moments points from the ITO surface to vacuum, and hence reduces the work function of the ITO surface. The degree of work-function reduction is determined by the magnitude of the dipole moment, which correlates to the V_{OC} variation, and is proportional to the electron-donating ability of the alkali-metal ions. With the inverted device structure (ITO/Cs_2CO_3 /RR-P3HT:PCBM/V_2O_5

/Al), the PCE improves from 2.31% to 4.19% by a thermal annealing treatment of the Cs_2CO_3
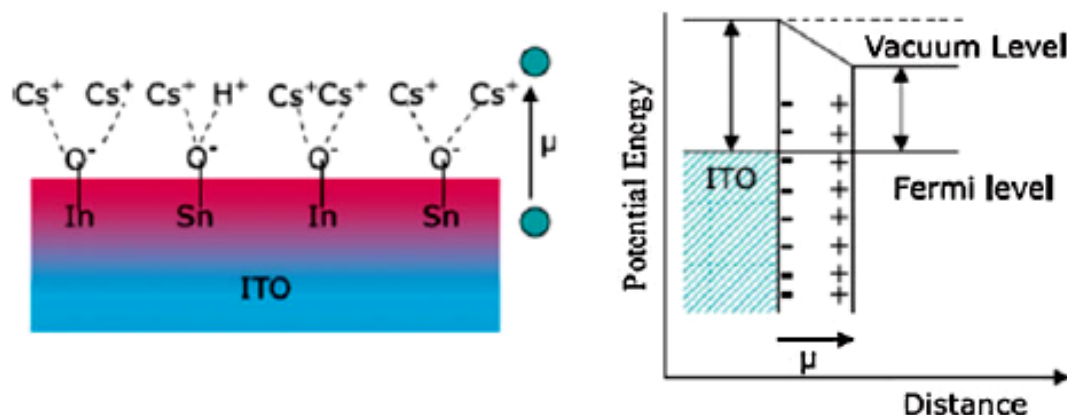
interfacial layer at 150°C.

Figure 4.2 : Scheme for the formation of dipole layer on ITO and its effect on reducing the

work function of ITO[55]

Besides the alkali metal compounds, nanocrystalline and amorphous transition metal

oxides, for example ZnO[54,55] and TiO_x[56,57], are solution-processible and also widely applied

in optoelectronics because of their low cost and nontoxicity. Moreover, comprehensive

research has established solid background knowledge on these two materials. Table 4-1

summarizes the device characteristics of some representative results regarding the inverted

structure polymer solar cells. It is seen that there kinds of materials, such as ZnO, TiO_x,

Cs_2CO_3, play important roles in forming a desirable film morphology and interface contact.

Table 4-1. Summarized results of the device characteristics from representative inverted polymer solar cells.[3]

Device structure	J_{SC} [mA cm^{-2}]	V_{OC} [V]	FF [%]	PCE [%]
ITO/Cs$_2$CO$_3$/P3HT:PCBM/V$_2$O$_5$/Al	8.42	0.56	62.1	2.25
ITO/ZnO/P3HT:PCBM/Ag	11.22	0.556	47.5	2.58
ITO/TiO$_x$/P3HT:PCBM/PEDOT:PSS/Au	9.0	0.56	62	3.10
ITO/PTE/TiO$_x$/P3HT:PCBM/PEDOT:PSS/Ag	10.2	0.56	64	3.60
ITO/ZnO NP/P3HT:PCBM/PEDOT:PSS/Ag	11.17	0.623	54.3	3.30
FTO/TiO$_2$/P3HT:PCBM/PEDOT:PSS/Au	12.40	0.641	51.1	4.07
ITO/annealed-Cs$_2$CO$_3$/P3HT:PCBM/V$_2$O$_5$/Al	11.13	0.59	63	4.19

Owing to the large band gaps and matching energy levels, ZnO is also suitable functional interfacial layer, since they can block the hole collection on the ITO side, thus inverting the polarity of the devices.

4.2 ZnO-Based Inverted Polymer Solar cell

4.2.1 ZnO Materials and Device Performance

ZnO thin films now attract significant attention due to their wide range of electrical and optical properties. They have potential application in electronics, optoelectronics and information technology devices including displays, solar cells and sensors[58],[59]. Several thin-film deposition techniques have been used to produce pure ZnO films, including sputtering[60], molecular beam epitaxy[61], metal-organic chemical vapour deposition[62], pulsed laser deposition[63], spray pyrolysis[64] and the sol–gel process[65],[66]. The sol–gel method has distinct potential advantages over these other techniques due to its lower crystallization temperature, ability to tune microstructure via sol–gel chemistry, conformal deposition ability, compositional control and large surface area coating capability[67,68]. The deposition of pure and

doped ZnO thin films by the sol– gel process has already been reported[69,70,71.] Previous report

has demonstrated that ZnO films strongly oriented along the (002) plane can be prepared on

silica glass substrates by using high temperature annealing from zinc acetate-2-

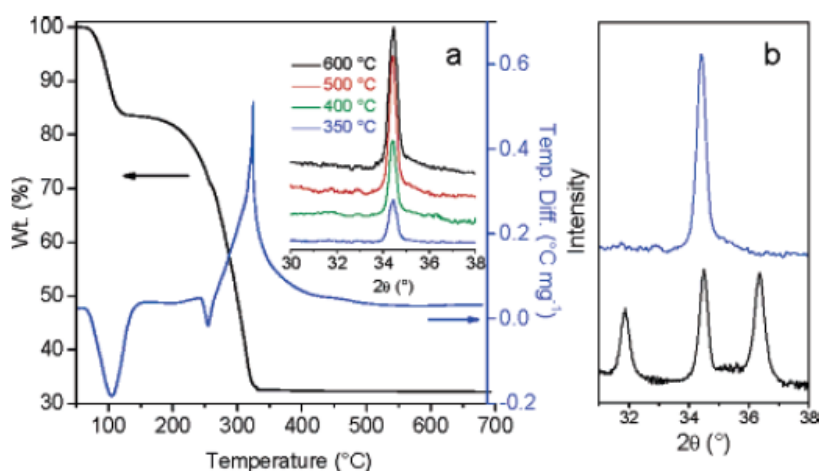methoxyethanol-monoethanolamine (MEA) solutions, as shown in Figure 4.3[72]

Figure 4.3 : (a) Thermogravimetric analysis (TGA) and differential thermal analysis of zinc

acetate dihydrate at 10 °C min^{-1} ramp rate. The inset shows XRD patterns of (40 nm) ZnO

films on ITO/glass, showing intensity of (002) peak (2θ=34.4°) increasing with increased

annealing temperature to ~500 °C, and then leveling off thereafter. (b) XRD patterns of a ZnO

film obtained by annealing from 25 to 500 °C at a heating rate, displaying three distinct peaks

at 31.9° (100), 34.4° (002), and 36.3° (101) (black line) and a ZnO film obtained by annealing

at 500 °C, showing essentially only (002) peak (blue line).[25]

In 2006, White et al. is the first one who incorporated high temperature annealing ZnO on ITO as the cathode buffer layer with silver as the anode and obtained a PCE of 2.58%.[73] Despite the different configuration, the V_{oc} is similar to those obtained from regular device structures (ITO/PEDOT:PSS/P3HT:P_{60}CBM/Ca/Al), which can be explained by Fermi-level pinning or dipole formation at the PCBM/ZnO interfaces. Importantly, an EQE maximum of almost 85% was achieved, indicating excellent internal quantum efficiency and overall charge-collection efficiency. The authors attributed the high EQE and J_{sc} to efficient hole collection at the P3HT/Ag interface, which is likely caused by the increased work function of oxidized Ag. However, they also noticed that degradation either in air or in inert environment (desorption of oxygen from ZnO) imposed stability issues on the ZnO-based devices.

ZnO is a large band-gap n-type semiconductor with a conduction band (CB) and valence band (VB) equal to 4.4 eV and 7.6 eV relative to vacuum, respectively. Similar to TiO_2, the conduction band edge of ZnO is lower in energy than that of the LUMO of (PCBM; 4.3 eV), which facilitates efficient electron transfer and extraction from the polymer:fullerene blend. In addition, the low-lying VB of ZnO can also effectively prevent hole carriers in the polymer from reaching the cathode. Other advantages are including its high electron mobility (0.066 cm^2V^{-1} s^{-1}) and solution processability. One key factor for improving the device performance of the inverted polymer solar cells is to reduce the series resistance, particularly the resistance of the functional buffer layer. It is well known that a high series resistance can

be reflected by the significant reduction in J_{SC} and FF.

4.2.2 Device with Modified ZnO

On the other hand, ZnO based polymer solar cells still have lower performance compared to TiO_x based devices. Therefore, two methods applied in the device to improve the interfacial engineering. The first one is to modify the ZnO surfaces with a self-assembled functional molecular layer. This method provides a versatile way to engineer the contact between the ZnO buffer layer and different active polymers. By using a spin-coating process to modify the ZnO NP interface of inverted solar cells with a C_{60}-SAM shown in Figure 4.4. The self-assemble monolayer (SAM) reduces the device series resistance by passivating the inorganic surface trap states as well as enhances the electronic coupling at ZnO/organic layer. It helps mediate forward charge transfer to reduce back recombination at the interface leading to improved FF and photocurrent densities. In addition, fabrication of these inverted devices in an inert environment was compared to those fabricated in a completely ambient environment to evaluate the differences in device performance (~4.4%).
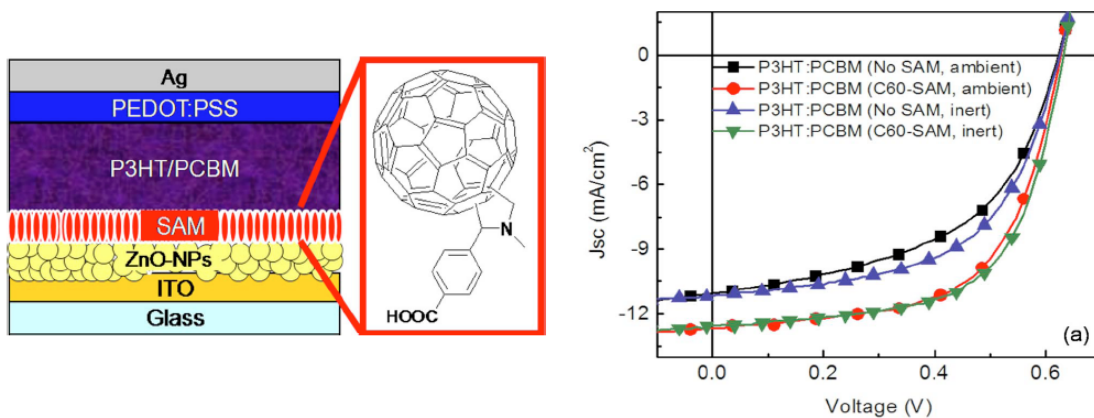
Figure 4.4 : (a) Device structure and chemical structure of inverted solar cell with C_{60}-SAM modification. (b) *J-V* characteristics of inverted ZnO NP/ P3HT:PCBM BHJ solar cells with and without C_{60}-SAM modification processed under inert and ambient environments.[74]

4.2.3 Device with ZnO Nanostructure

Another useful method to improve the device performance is to apply one dimensional structure such as nanorod[75], which has been investigated since 2005, it can avoid the incomplete exciton dissociation due to non-ideal dispersion of the nanoparticles in the blend and low carrier mobility through the nanoparticle pathways in the blend. Similar hybrid devices have been prepared from metal oxide precursors and conjugated polymers, where the metal oxide precursor is transformed after the composite film has formed resulting in a metal oxide/ conjugated polymer composite device. It was shown that ZnO nanoparticles demonstrated better performance than TiO_2 nanoparticles.[27] However, these devices are still limited by incomplete exciton dissociation and the polycrystalline nature of the metal oxide. A nanostructured oxide that is vertically aligned with respect to the substrate offers a

48

promising means to increase the efficiencies of these devices. ZnO is a good candidate for this application as preferential growth of single-crystal ZnO fibers from a nucleation layer has been demonstrated to be in the (001) direction, normal to the substrate. This increases the donor-acceptor interfacial area and creates high mobility electron transport pathways connected only to the negative electrode. Moreover, dye-sensitized solar cells have been fabricated using ZnO nanowire anodes with efficiencies have demonstrated improved electron transport and electron injection in single-crystal nanowires over polycrystalline networks of sintered ZnO nanoparticle films.

A schematic of a composite device based on vertically aligned nanostructures is presented in Figure 4.5. This structure has been demonstrated successfully to apply in the inverted polymer solar cell and obtain PCE of 3.9%.
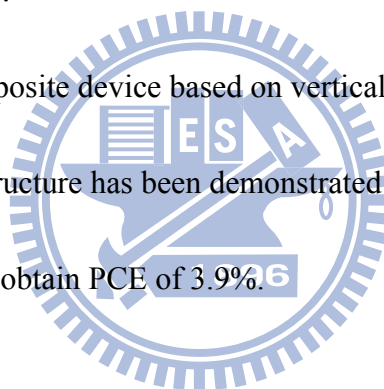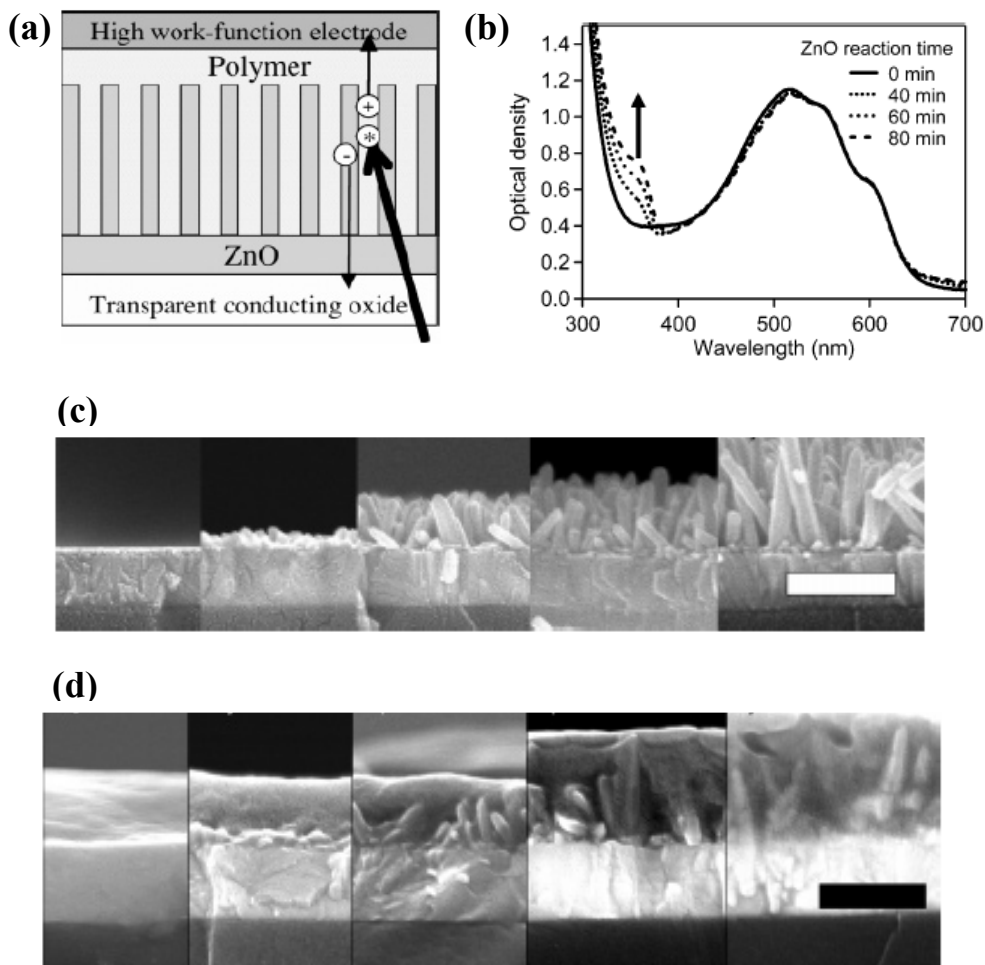
Figure 4.5 : (a) Schematic diagram of an ideal nanostructured oxide/ conjugated polymer photovoltaic device.(b) Absorption spectra of the P3HT:PCBM films on the array of the ZnO nanorods. The ZnO crystal growth time was changed from 0 to 80 min.(c) FE-SEM cross section images of ZnO nanorod on ITO with different crystal growth time. (d) FE-SEM cross section images of the P3HT/PCBM layer spin-coated on the ZnO nanorods.[76]

Inspired by these works on ZnO-based inverted solar cells, we focus on the morphology control, emphasizing on a series of key parameters for film evolution, such as growth, defects and nanostructures with annealing treatment.

The chapter 4,5 give an in-depth discussion of the optical, chemical and electrical properties of ZnO as the electron transport layer in tandem cell and designed to be the effective interlayer with other p-type materials. As an emerging topic, the current status of the single inverted polymer solar cells and inverted tandem solar cells are presented in the following chapters.

4.3 Device Structure Design and Experimental Details

As mentioned, the function of either ZnO nanorod or the modified-ZnO nanoparticles by SAM is obvious, however, the sensitive material properties of nanostructures, more complicated preparation and conditions are therefore difficult to control the quality precisely and repeatedly. Therefore, we designed a simple annealing process to achieve a nano-ridge structure, which has improved hole blocking and electron collection properties. The fabrication of sol-gel processed ZnO nanoparticle films with planar and nano-ridge structures were made from spin coating the same precursor solution but annealing under different conditions. The precursor solution, consisting of 0.75M zinc acetate dihydrate and 0.75M monoethanolamine in 2-methoxyethanol[77], was first spun-coated onto indium tin oxide (ITO) substrates at 2000rpm for 40s. For the ZnO planar film, the substrate was immediately placed onto a hotplate that was preheated at 275 ^{o}C for 5min. In order to form the ZnO nano-ridge film, the spin-coated substrate was first placed onto a hotplate that was initially at room temperature while it was still not completely dry. The temperature was then raised at a

ramping rate of 50 °C/min to 275 °C and the substrates were subsequently removed from the

hot plate when the final temperature was reached. Quartz substrates were used when

measuring the transmittance of the ZnO films. The resulting ZnO films were rinsed in

de-ionized water, acetone, and isopropyl alcohol and then dried to remove residual organic

material from the surface. All processes thus far were done in ambient air. The substrates

were then transferred into a nitrogen-filled glovebox for polymer coating. P3HT /PCBM

blend films were spun-coated onto the substrates from a 1:1 wt-ratio solution in 1,2

dichlorobenzene (20mg of P3HT/ml of solvent) at 600 rpm using the slow-growth method[1],

followed by annealing on a hotplate at 110 °C for 10 min. To complete the solar cell devices,

a 10nm layer of V_2O_5 (serving as a buffer layer for hole collection[78]), following by 70nm of

Ag was deposited by thermal evaporation through shadow masks. The device area, as defined

by the overlap between the ITO and Al electrodes, was 0.09cm^2. The solar cells were

measured under simulated illumination at AM 1.5G, 100mW/cm^2 with a Keithley 2400 source

meter controlled by a computer program.

4.4 Results and Discussions

The schematic device structure and the scanning electron microscopy (SEM) images of

the device and the ZnO nano-ridge structured film are shown in Figure 4-6 and Figure 4-7
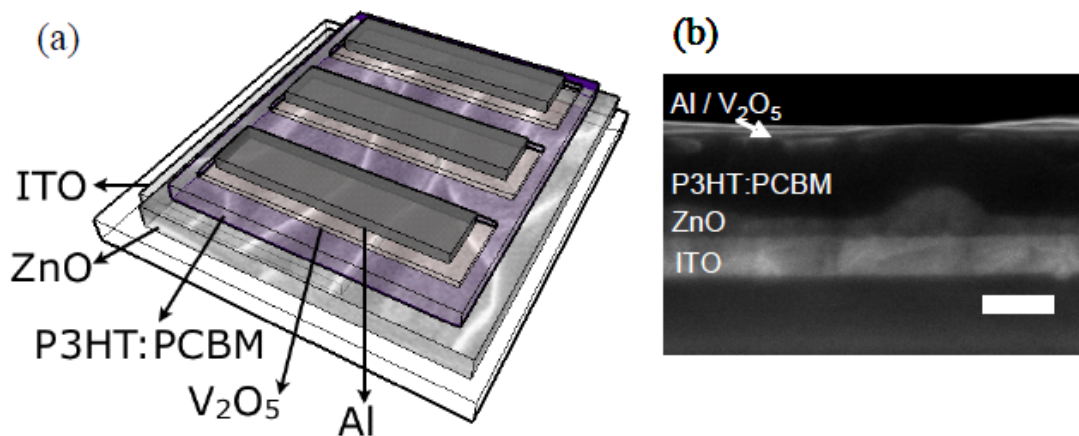
Figure 4.6 : (a) Device structure, (b) SEM cross-sectional image of the inverted polymer

solar cell, scale bar : 200 nm
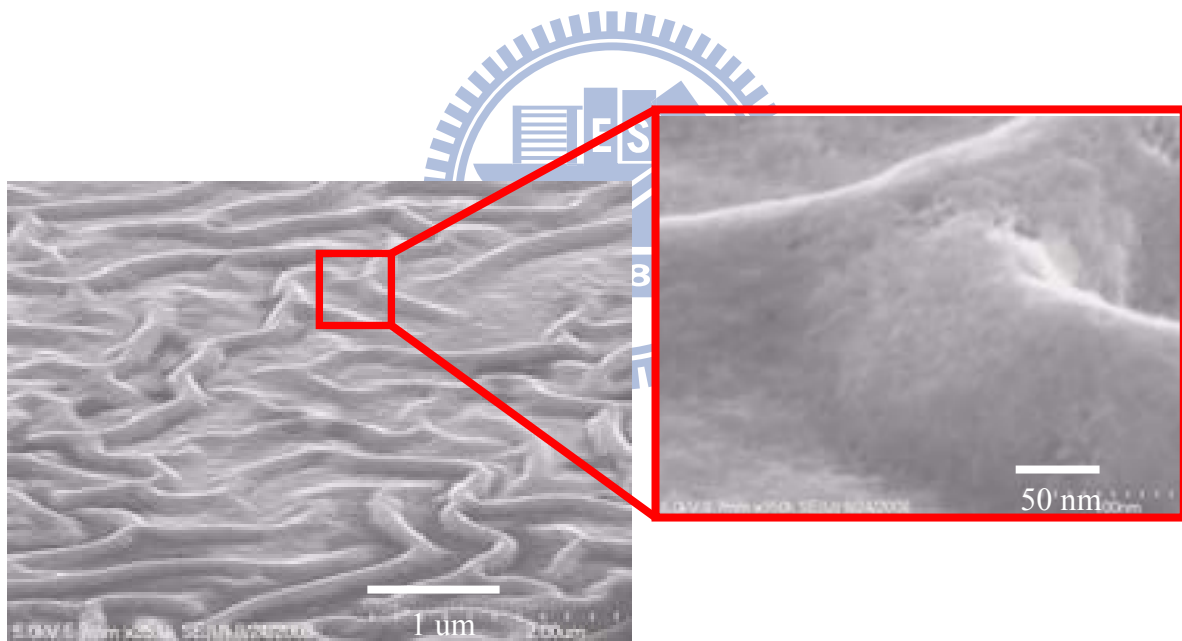

Figure 4.7 : SEM image of the ZnO nano-ridge film,

The atomic force microscope (AFM) images of the nano-ridge and planar films are

shown in Figure 4.8(a) and (b), respectively. Nano-ridges of ZnO nanoparticles with thickness

ranging from 50nm to 120nm were formed and the valley to valley distance of the

nano-ridges was about 500nm. The ZnO nano-ridge structure was formed by the

reorganization of gel particles during the slow drying process[79,80]. The ZnO planar film was relatively smooth with an r.m.s. roughness of about 2.6nm. Figure 4-8. (c) and (d) shows the close up AFM images of the nano-ridge and planar films respectively.
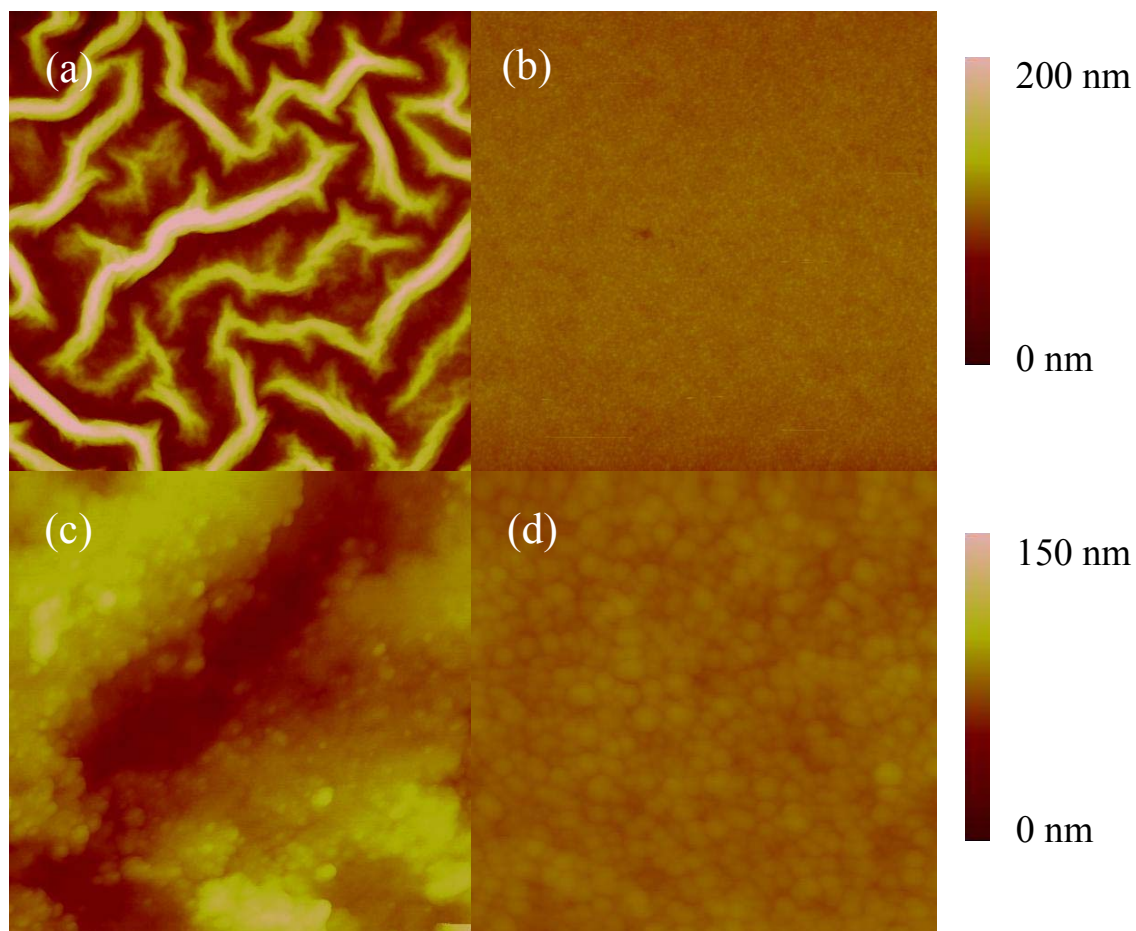

Figure 4.8 : AFM images of the (a) ZnO nano-ridge and (b) ZnO nanoparticle planar films showing a 5 μm×5 μm surface area. Close-up AFM images of ZnO nano-ridge(c) and ZnO nanoparticle planar(d) films showing a 500nm×500nm surface area

The transmittance spectra of the ZnO films and absorbance of the ZnO films coated with P3HT:PC$_{60}$BM are shown in Figure 4.9. The ZnO nano-ridge film had a slightly lower transmittance over a broad range of wavelengths as compared to that of the ZnO planar film. This was due to the increase in light scattering by the nano-ridges and was consistent with the white foggy appearance of the film[81]. The polymer films with both types of ZnO morphology showed very similar absorption. All the films show the same optical density of 0.77 at 510 nm regardless of the ZnO layer, which corresponds to the organic layer thickness of 200 nm in a flat film. This result indicates that the same amount of the polymer can be deposited on the ZnO substrates for all the samples under the same coating condition. At the same time, the transmittance around 360 nm corresponding to the absorption of ZnO increased as the peak to valley of the nano-ridge increased as indicated by an arrow in Figure 4.9. From the results shown above, we conclude that the films can be divided into two regions: the organic/ZnO nanorod hybrid layer on the ITO and the pure organic layer on the top, as shown in Figure 4.6a. Since the absorption (i.e., the amount) of the organic components is the same for all the films regardless of the thickness of nano-ridge, direct comparison of the device performance is possible in the following sections.
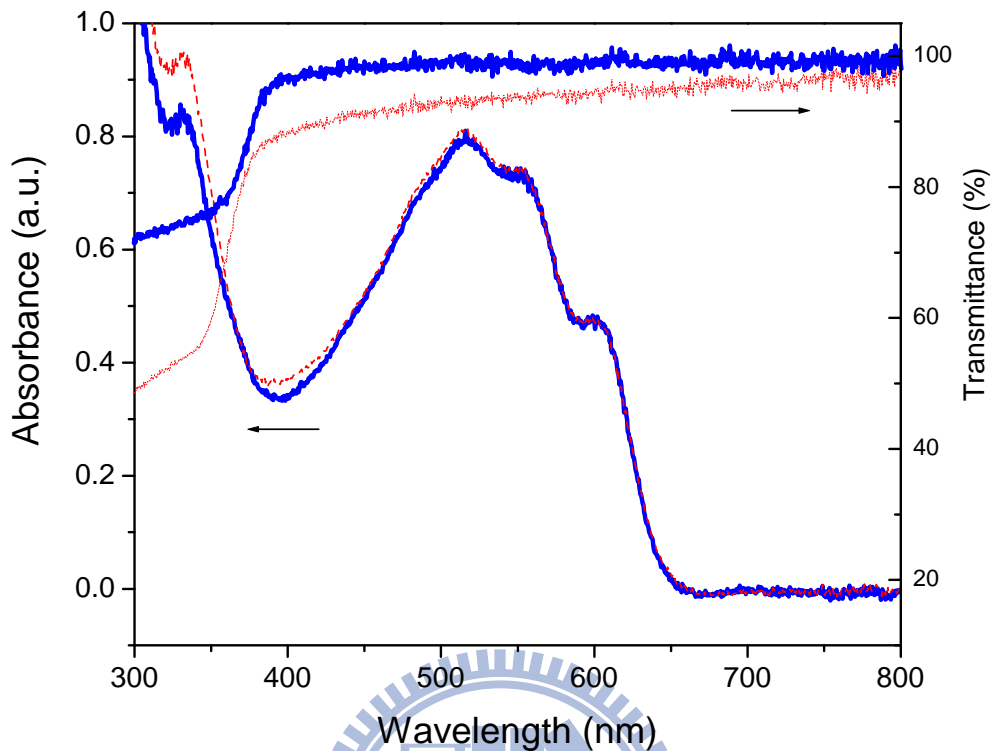
Figure 4.9 : The absorbance spectra for P3HT:PCBM on ZnO nano-ridge film (dotted

line) and planar film of ZnO nanoparticles (bold line) and the transmittance spectra of

the nanoridge film (dotted line) and planar film (bold line)

The current-voltage (J-V) characteristics of the solar cell devices with ZnO nano-ridge

and planar films under simulated sunlight were shown in Figure 4.10. The device

performance is summarized in Table 4-2. The ZnO nano-ridge device showed a remarkable

improvement over the device with the planar film. The major improvement in device

performance arises from the higher fill factor (FF) of the ZnO nano-ridge device, while the

open circuit voltage (V_{oc}) and short-circuit current density (J_{sc}) remained almost unchanged.

We attributed this enhancement to lower leakage current due the improvement in hole blocking capability and electron collection efficiency of the nano-ridge structured film.
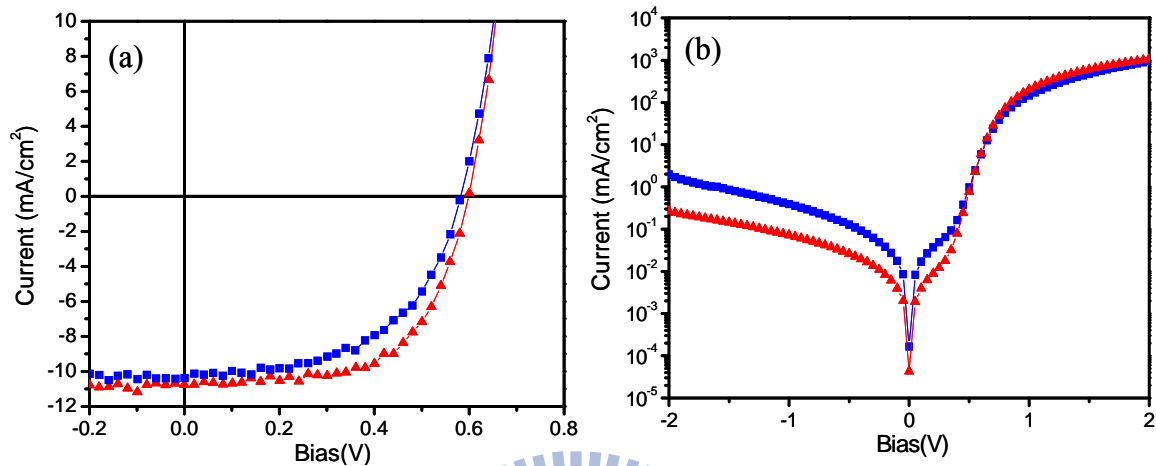

Figure 4.10 : (a) Current density-voltage (J-V) curves of the ZnO nano-ridge (triangle) and ZnO nanoparticles (square) devices under 100 mW/ cm^2 AM1.5 irradiation (b) Dark J-V curve of the same devices.

The dark J-V curve (Figure 4-10b.) shows a lower leakage and higher forward bias current for the ZnO nano-ridge device, indicating better charge selectivity over the ZnO planar film. This is due to the difference in the packing density of the films. As the ZnO nano-ridge film is formed by a slower heating process, there is sufficient time for the gel film to structurally relax before crystallizing, resulting in a denser film[30] than that of ZnO planar film[29]. A denser film with fewer defects would be more effective in blocking the transport of holes, leading to lower leakage current, i.e. a larger shunt resistance and higher FF. The shunt resistance

showed a change of about an order of magnitude while the series resistance remained almost

unchanged. It is unlikely that the improvement in the device performance is due to the change

in carrier concentration or work function.

To clarify whether the nano-ridge structure of the ZnO played a role in improving

charge extraction, bilayer devices without $PC_{60}BM$ were also fabricated. The J_{sc} for the ZnO

nano-ridge bilayer device was close to two times higher than that of the device with the ZnO

planar film, indicating a much larger interfacial area for charge separation. Similar to the

results of ZnO nanorods[82] we believe that our ZnO played a comparable role, albeit a smaller

one, to that of the ZnO nanorods-based solar cells. The larger surface area of electrode contact

and undulate network structure minimized the distance charge carriers need to travel in the

active polymer to reach the electrodes.

Table 4-2　The device performance of ZnO nanostructure based inverted polymer solar cells

ZnO structure	Active Polymer	Voc (V)	Jsc (mA/cm^2)	PCE (%)	FF (%)	R_s/Ω (cm^2)	R_p/Ω (cm^2)
NP	P3HT	0.79 (0.80)	0.18 (0.19)	0.05 (0.06)	42 (44)	4.26e^4 (4.60e^4)	15.3 (15.0)
NR	P3HT	0.74 (0.74)	0.35 (0.37)	0.14 (0.15)	55 (56)	1.06e^5 (1.11e^5)	14.5 (14.3)
NP	P3HT:PCBM	0.58 (0.58)	10.35 (10.41)	3.06 (3.20)	51 (53)	1.77e^4 (2.30e^4)	1.6 (1.4)
NR	P3HT:PCBM	0.60 (0.60)	10.57 (10.76)	3.87 (4.00)	61 (62)	1.11e^5 (1.42e^5)	1.5 (1.4)

NP : nanoparticle ;　NR: nano-ridge

4.5 Summary and Conclusions

We reported a ZnO nano-ridge structured film that can be formed by a simple ramp annealing process. The nano-ridge structure has comparable excellent electron collection properties as that of ZnO nanorods and yet can be made with similar simple fabrication processes as the ZnO planar film. The effect of the viscosity of the solution and the solvent evaporation rate on the nano-structured pattern is to be further studied. Both inverted bulk heterojunction polymer solar cells and ZnO:P3HT hybrid solar cells showed remarkable improvements in efficiency when the ZnO nano-ridge structure was used. We attributed the improvement in FF to higher electron selectivity and more efficient charge collection, leading to a 4.0% inverted polymer solar cell.
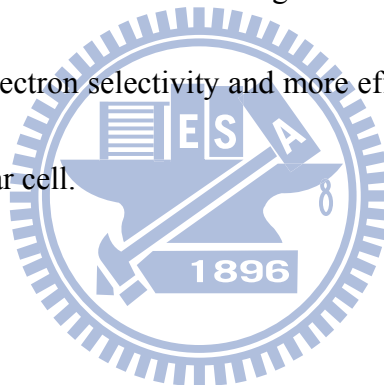
Chapter 5

Highly Efficient ZnO-Based Inverted Tandem Polymer Solar Cell

5.1 Background and Motivation

The emerging field of stacked layers (double- and even multi-layers) in organic solar cells has been reported. Owing to the limited absorption width of organic molecules and polymers, only a small fraction of the solar flux can be harvested by a single BHJ solar cell. Furthermore, the low charge-carrier mobilities of most organic materials limit the thickness of the active layer. Consequently, only part of the intensity of the incident light at the absorption maximum is absorbed. A tandem solar cell, consisting of multiple layers each with their specific absorption maximum and width, can overcome these limitations and can cover a larger part of the solar spectrum. Moreover, tandem cells provide the distinct advantage of using photon energy more efficiently, because the voltage at which charges are collected in each cell is closer to the energy of the photons absorbed in that cell.

When the two cells are connected in series, the total generated photocurrent will be constant throughout the device. Furthermore, the voltages generated by the cells will add up. As a result for each point of the J–V characteristic of the tandem device the following relations are valid,

$J_{Tandem} = J_{Bottom} = J_{Top}$ (1)

$V_{Tandem} = V_{Bottom} + V_{Top}$ (2)

Graphically, Eq. (1) means that we can draw an arbitrary horizontal line through Figure 6-1, indicating a chosen constant current density that flows through the cells. This horizontal line crosses the J–V curves under illumination of the individual bottom and the top cell at a specific voltage for each sub cell. Those cross-points are the values of the voltages with which the sub cells are effectively biased in order to generate the chosen constant current density. Eq. (2) then shows that we have to add those two voltage values in order to determine the bias voltage of the tandem cell in series at that constant current density. The re-plot of Figure 5.1 exhibits between zero and ~10 A/m^2 in order to enlarge the vertical axis and choose three arbitrary current densities as shown in Figure 5.2
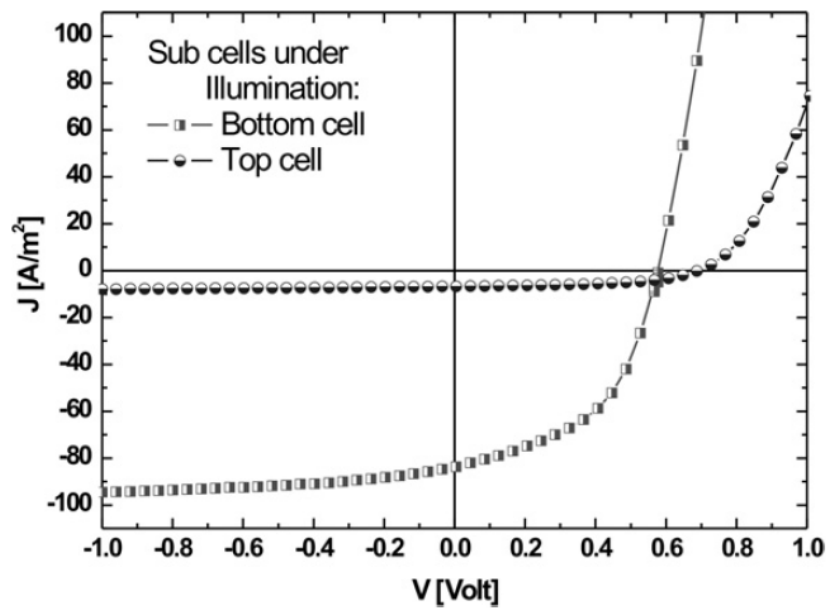

Figure 5.1: The J-V characteristic of two cells under illumination. The top cell delivers higher open-circuit voltages, while its photocurrent is much lower than the bottom cell[83]

The horizontal line 1 is the open-circuit condition for both sub cells in which the current densities in both of them are zero (cross-points A and B). Line 2 shows the short-circuit condition of the top cell (cross-point C), whereas the bottom sub cell is biased by a positive voltage (cross-point D). Line 3 is the condition in which the bottom cell is biased by a positive voltage (cross-point F), whereas the top is biased by a negative voltage (cross-point E)
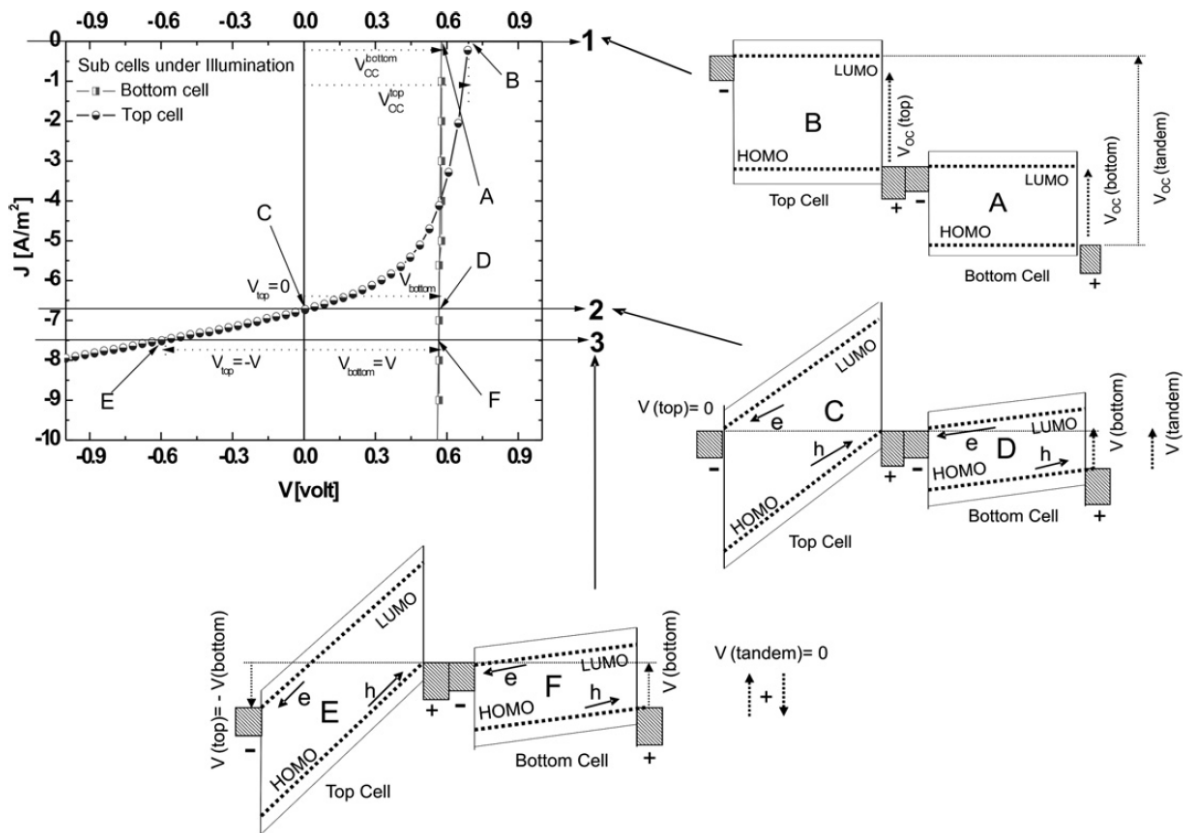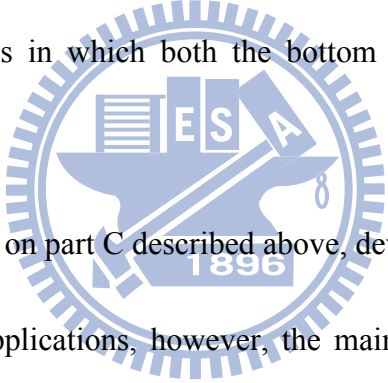

Figure 5.2: A close-up of the vertical axis of Figure. 6.1 between 0 and 10 A/m^2. The horizontal lines 1–3 cross the curves of the bottom (A, D and F) and top cells (B, C and E), indicating a constant current density. For each line the energy-band diagrams are given[1]

5.2 Recent Developments

Several approaches for organic tandem cells have been reported in the past 3 years, depending on the materials used for the active layer and the proper separation or recombination layer(s). All layers can be different in each architecture or approach. In general, the multiple organic solar cells can be divided in three classes: (A) Tandem cells in which low-molecular-weight molecules are used for both the bottom and the top cells. (B) Hybrid tandem cells in which the bottom cell is processed from polymers by solution-processing while the top cell is made of vacuum-deposited low-molecular-weight molecules. C) Fully solution-processed tandem cells in which both the bottom and the top cells are made of polymers

In this section, we focus on part C described above, developing the all solution process tandem cells for large scale applications, however, the main problem in the fabrication of polymer tandem cells is the stack integrity: deposition of the top cell might dissolve or damage the earlier deposited bottom cell, especially when similar solvents as chlorobenzene (CB) and chloroform are used. Therefore, a separating layer is required that has to be thick enough to protect the bottom cell from dissolving during spin coating of the top cell. At the same time, the separating layer has to be as transparent as possible to transmit light efficiently to the top cell.

To overcome the stack integrity problem, different structures and methods have been reported recently. The most recent and efficient tandem cell with PCE of 6.5% based on

solution processing was reported by Kim et al.[84] A transparent titanium oxide (TiO_x) layer is used to separate the two cells of the tandem device. Similar to the approach by Gilot et al.[85] but now using this transparent TiO_x middle electrode, also fully solution-processed tandem cells can be realized. The advantages of using oxides such as the above-mentioned ZnO or TiO_x for the middle electrode is the optical transparency of the layer and the orthogonally compatible solvents used for processing all layers.

In these cases, the separating layer does not significantly affect the light intensity. This high light intensity at the top cell leads to a high photocurrent generated by the top cell. Therefore, the efficiency of the tandem device is not limited any more by the lower current of the top cell as observed for tandem structures with metallic interlayer[86]. The cell was processed onto glass/ITO substrate covered by 40 nm thick layer of PEDOT:PSS (Baytron P). The transparent $TiOx$ interlayer is fabricated by spin coating from methanol solution by means of sol-gel chemistry. For the bottom BHJ cell a 130 nm thick layer of PCPDTBT:PCBM (1:3.6) was used and processed from chlorobenzene. The top BHJ cell is fabricated from 170 nm thick P3HT:PC$_{70}$BM (1:0.7) blend which was processed from chloroform. The two sub-cells have complementary absorption spectra, which leads to coverage of the whole visible and part of the infrared spectrum by the tandem device. On top of the $TiOx$ interlayer layer, the highly conductive hole transport layer PEDOT:PSS (Baytron PH500) was spin coated. The basic structure of the device is given in Figure 5.3
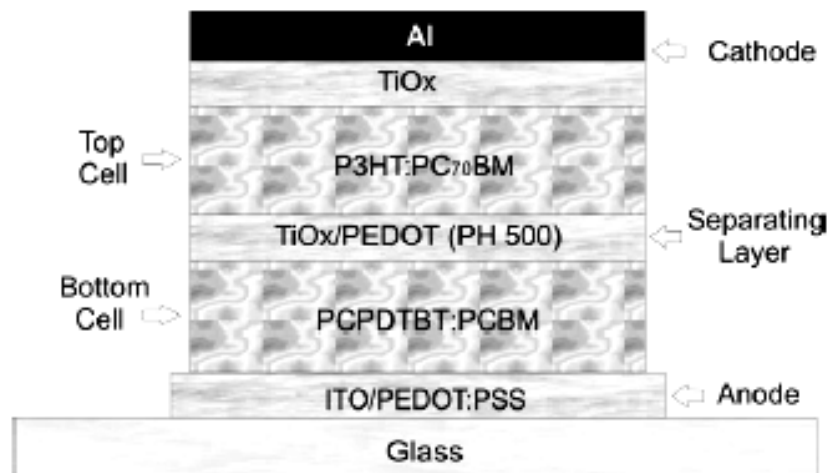
Figure 5.3 : The structure of tandem device in which the two cells are separated by a highly transparent layer of TiO_x covered by the highly conductive PEDOT:PSS[4].

Very recently, Sista et al.[87] reported the detailed working mechanism of the interlayer that joins the two sub-cells in a tandem cell. The role of the n-type and p-type layers constituting the interlayer and several important issues of the tandem structure was studied, including optical optimization, interfacial engineering and accurate efficiency characterization. A deeper insight into the interlayer, consisting of a n-type nanocrystalline TiO_2 layer and a p-type conducting PEDOT:PSS layer, reveals that it acts as a metal-semiconductor contact as opposed to a tunnel junction in inorganic tandem cells. Making use of an efficient interlayer, we have demonstrated high efficiency tandem cells with power conversion efficiencies of 5.8%. Furthermore, a high conductivity interlayer should be avoided for accurate device

efficiency characterization, which otherwise leads to overestimation of efficiencies by as much as 10%. The understanding developed in that paper can be extended to large band gap polymers that can deliver higher V_{oc} and hence further enhance the tandem cell efficiencies.

Figure 5.4(a) and (b) shows the device configuration and the proposed energy level diagram of the tandem cell, respectively. Figure 5.4(c) suggests that over 70% of incident light is absorbed by the film when a reflective cathode is used. Optical simulation was performed to calculate absorption profile for matching the absorption balance between the two cells. Figure 5.4d shows the optical simulation results that a 100-nm HSi:PC$_{71}$BM film is estimated to be sufficient to absorb 15% more number of photons than the front P3HT:PC$_{71}$BM cell under illumination of AM1.5G solar spectrum.

The highly efficient regular tandem solar cells have been reported above, however, for inverted tandem cell, is still lack due to the improper design for interlayer and technical problem. In the following section, we will describe in-depth discussion of the optical, chemical and electrical properties of interlayer design for highly efficient inverted tandem cell
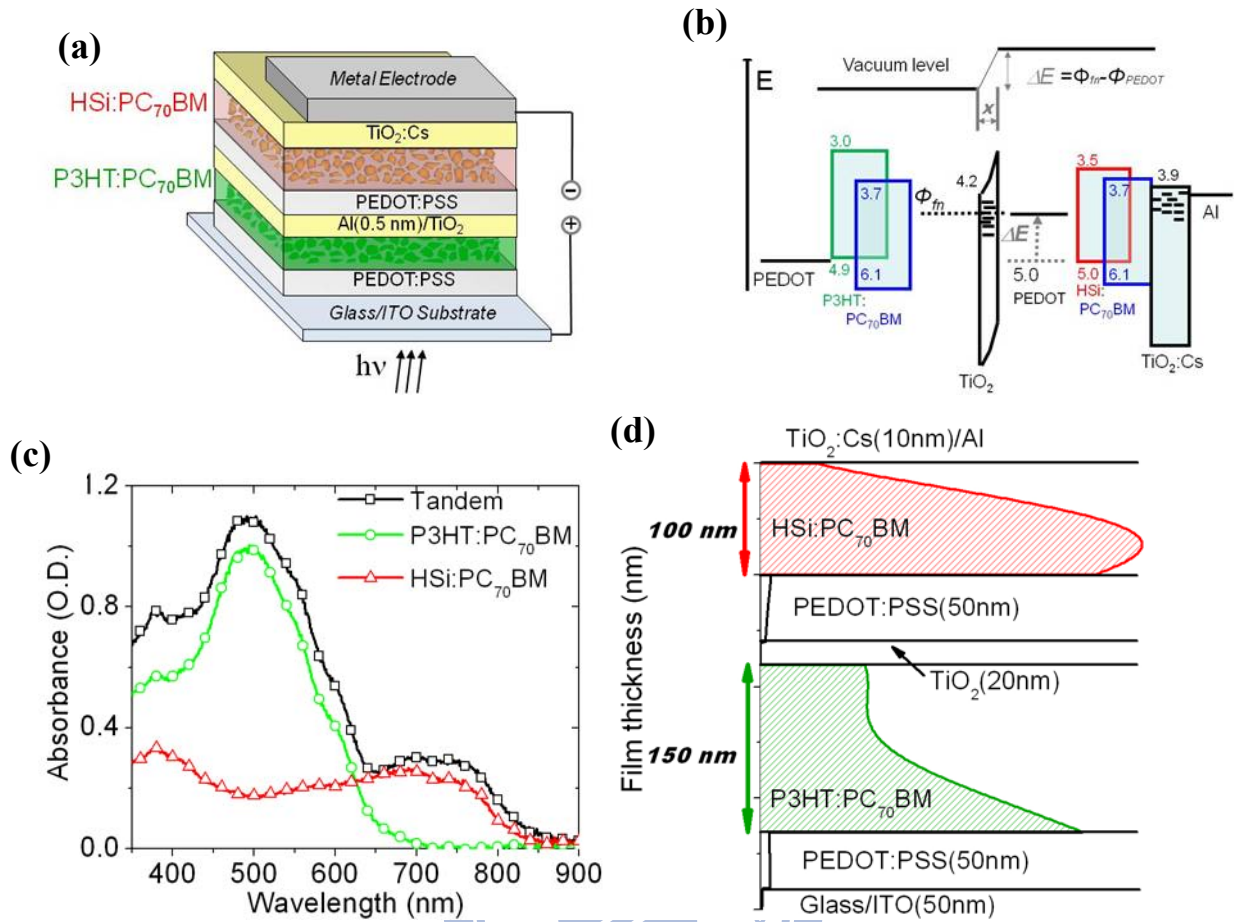
Figure 5.4 : (**a**) Device configuration and (**b**) proposed energy level diagram of tandem solar cells containing two BHJs as sub-cells and TiO$_2$/PEDOT4083 as inter-connection layer. (**c**) absorbance (optical density, i.e. O.D.) of P3HT:PC$_{71}$BM and HSi:PC$_{71}$BM BHJ films, and tandem photovoltaic cells in absence of metal cathode. (**d**) Calculated absorption profile of the tandem cell under AM1.5G spectrum illumination. Integration of the absorbed number of photon for the two sub-cells indicates that the top cell has overall absorption 15% larger than the bottom cell.

5.3 Device Structure Design and Experimental Details

Tandem polymer solar cells have attracted considerable interests due to their potential for higher device performance. However, efficiency and stability are important problems that remain to be solved. To overcome the compromise between absorption and transport properties of polymer BHJ solar cells, it is desirable to stack individual cells with complementary absorption in a tandem structure. To improve the stability of polymer solar cells, devices with inverted structure have been proposed. In the inverted solar cell, as described in chapter 4 the reactive low work function metal is replaced by an inorganic electron collection layer which includes $CsCO_3$[88], TiO_2[89], TiO_2:Cs[90] and ZnO[91]. The device is capped with a hole collection layer and a stable high work function metal. The positions of the anode and cathode are also reversed. Besides having better stability, it also takes the advantage of the favorable vertical compositional profile of the polymer blend.[92]

In this section, we report a highly efficient inverted polymer tandem solar cell which combines the benefits of the extended absorption of a tandem cell and the stability of an inverted structure. In the tandem structure, the interlayer connecting the top and bottom polymer films plays the role of the charge recombination layer. For the V_{oc} of the top and bottom sub-cells to add together in the tandem cell, the interlayer has to provide an ohmic contact for charge extraction from both sub-cells. Therefore, most interlayers reported thus far consist of at least two layers, one for collecting electrons from the bottom cell and one for

collecting holes from the top cell. Various interlayers consisting of different combinations of metals, polymer, and inorganic materials have been reported[1-4,93]. An effective interlayer has to possess the following properties: (1) high optical transparency, (2) good electrical contact to both sub-cells, (3) robustness to protect the underlying layers against solvent. It is also important to select a suitable deposition technique which is compatible with the materials used.

For tandem cells with an inverted structure, the sequence of depositing the interlayer has to be reversed, giving rise to new processing issues that need to be solved. To date, there has no effective interlayer for inverted tandem cells. Herein, we will discuss the challenges with respect to materials selection, processing of the interlayer and the strategies we took to overcome them.
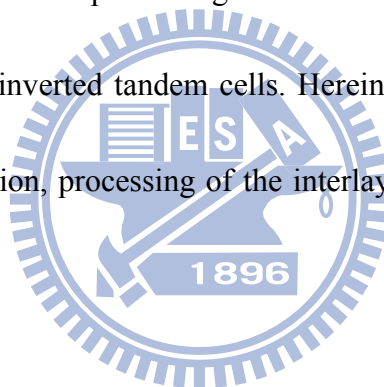
The device architecture of the individual layer in inverted tandem cell is shown in Figure 5.5. The fabrication of our tandem cells on glass substrates coated with transparent conducting indium tin oxide (ITO) of a sheet resistance of $15\Omega/cm^{-2}$. The ITO substrates were treated with UV/ozone prior to spin-coating amorphous ZnO layer at 4000 rpm for 40 sec, the mixed precursor solution consisting of 0.5M zinc acetate dehydrate in 0.5M monoethanolamine (MEA) and 2-methoxyethanol as described previously[1], following by baking at 150 °C for 5 minutes in ambient air. The resulting ZnO-coated cathode were rinsed

in de-ionized water, acetone, and isopropyl alcohol and then dried to remove residual organic

material from the surface, then transferred into glove box for polymer deposition. The first

layer was spin-coated from P3HT:P_{60}CBM blend films via slow-growth method[1] from a 1:1

wt:ratio solution in 1,2 dichlorobenzene (15mg of P3HT/ml of solvent) at 600 rpm with

annealing at 110 °C for 10 min, then subsequently thermal evaporating a layer of 10 nm

MoO_3/ 1 nm Al as the anode. This anode can be constructed similarly with the amorphous

ZnO layer at 4000 rpm for 40 sec, the mixed solution consisting of 0.3M ZnO precursor

solution with annealing at 150 °C for 5 minutes in ambient air as the cathode for top cell,

forming the robust interlayer and following the same rinse procedure as first ZnO layer on

ITO. The second active layer was spin-coating at 4500 rpm for 30 sec from PSBTBT:PC_{70}BM

in chloroform and thermal annealing at 150^0C for 5 minutes. Finally, to complete the solar cell

devices, a 10nm layer of MoO_3 and 70nm aluminum anode deposited by thermal evaporation

through shadow masks. The device area, as defined by the overlap between the ITO and Al

electrodes, was 0.09cm$^{2.}$ All the electrical measurements were performed in a nitrogen filled

glove box at room temperature.

5.4 Results and Discussions

The device architecture for the optimized inverted polymer tandem solar cell is depicted in Figure 5.5(a). The interlayer consists of MoO_3 (10nm) and ZnO (30nm) films acting as hole and electron collection layers respectively. An ultra thin layer of Al was inserted between MoO_3 and ZnO. The thickness of the Al is estimated to be ca. 1nm by the thickness monitor during the thermal evaporation process. The role of this Al layer is discussed below.

As shown in Figure 5.5(b), the transmittance (T%) of the MoO_3/Al/ZnO interlayer is almost 95% from 350 to 850 nm. The high transparency ensures minimal optical loss due to the interlayer. For the active layers, we selected two polymers which have complementary absorption. The overlapping absorption spectra of the (P3HT): ($PC_{60}BM$) blend, and (PSBTBT): ($PC_{70}BM$) blends exceed 0.8 optical density from 350-600 nm, whereas the absorbance reaches 0.3 at 750 nm, corresponding to the absorption of the rear cell. This suggests that over 50% of the incident light is absorbed by the films when a reflective cathode is used.
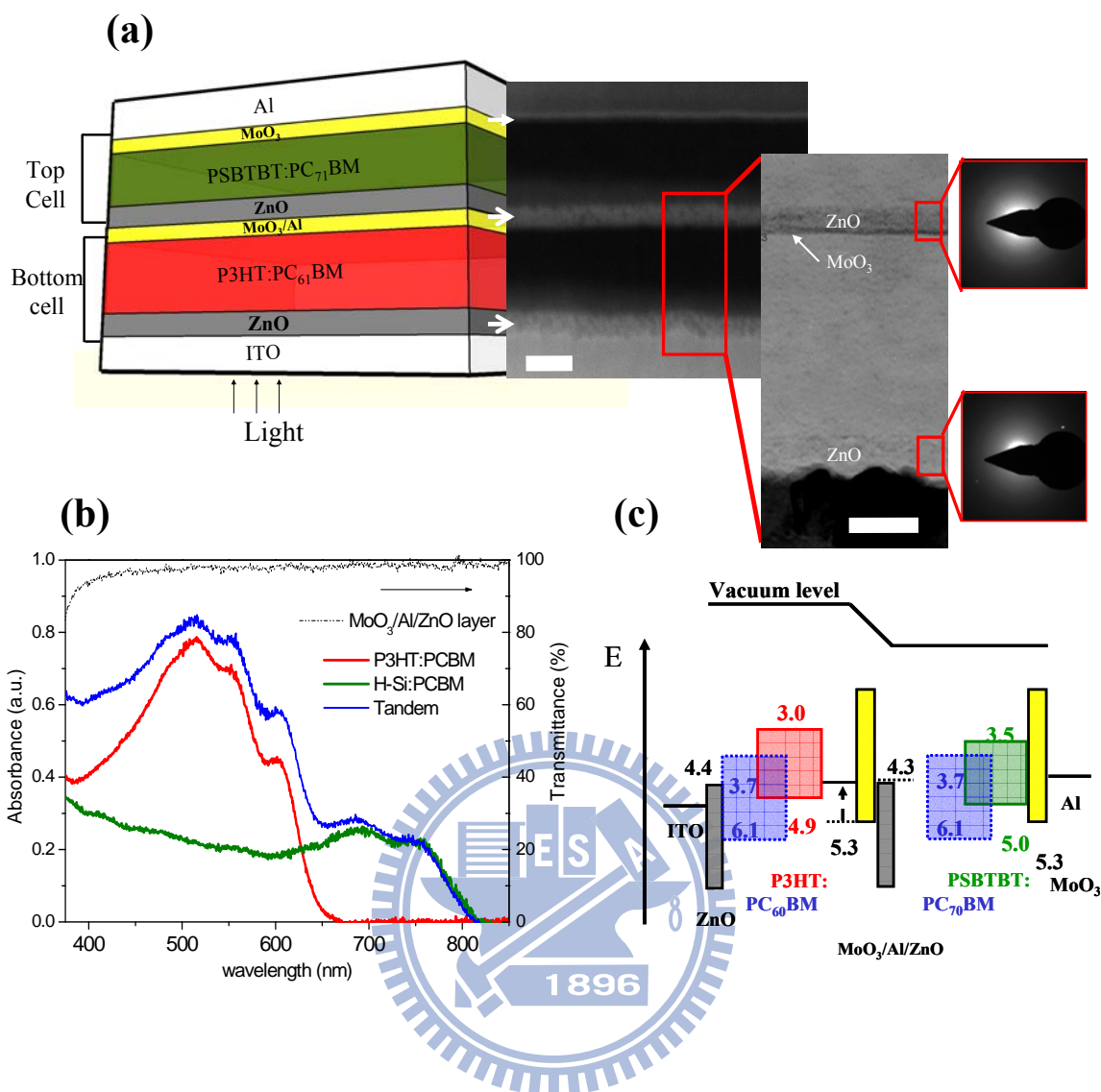
Figure 5.5 : (a) The device structure (left) and TEM cross-sectional image (right) of the inverted polymer tandem solar cell. Scale bars, 100 nm. (b) Absorbance (optical density, i.e. O.D.) of P3HT:PC$_{70}$BM and HSi:PC$_{70}$BM BHJ films, and tandem photovoltaic cells in absence of metal cathode (c) Energy-level diagram showing the HOMO and LUMO energies of each of the component materials.

Cross-sectional images (Fig. 5.5a) of the tandem cell by FE-SEM and TEM show very well-defined individual layers. The bottom cell is fabricated from P3HT: PC$_{60}$BM blend, with optimal thickness of 150 nm. The thickness of the top cell, which consisted of

PSBTBT:PC$_{70}$BM blend, was 120 nm. Figure 5.5(c) shows the energy levels of each layer.

The performances of the tandem cells and reference sub-cells under simulated solar illumination of AM 1.5G (100mW/cm^2) are shown in Figure 5.6(a). The tandem cell yields a power conversion efficiency (PCE) of 5.1%, with V_{oc} = 1.2 V, J_{sc} = 7.8 mAcm^{-2}, and FF = 54%. P3HT:PC$_{60}$BM single cell yields a PCE of 3.2%, with Voc = 0.58 V, J_{sc} = 8.57 mAcm^{-2}, and FF = 64%. The low band-gap PSBTBT:PC$_{70}$BM cell exhibits a PCE of 3.7%, Voc = 0.64 V, J_{sc} = 11.7 mAcm^{-2}, and FF = 49% . The Voc of the tandem cell is equal to the sum of the Voc of each sub-cell, confirming the successful coupling of the two cells in series.

The external quantum efficiency (EQE) measurement for the tandem and reference cells was performed and the results are shown 4-6(b). The EQE spectrum of the P3HT: PC$_{60}$BM reference cell has an average value over 50% throughout the visible range due to strong absorption of both P3HT and PC$_{60}$BM. Photoresponse of the reference rear cell is consistent with the previously reports[94], showing a broad response range from 350 nm to 800 nm with a maximum of over 40% at 700 nm. Integrating the EQE spectra of the single cells and sub-cells of the tandem cell yields Jsc values in good agreement with those obtained from the J-V curves shown in Figure 5.6(a). As shown, the interlayer provided an optimized coupling between the two sub-cells without any optical or electrical losses. We will elaborate on the materials selection and the optimization of this interlayer.

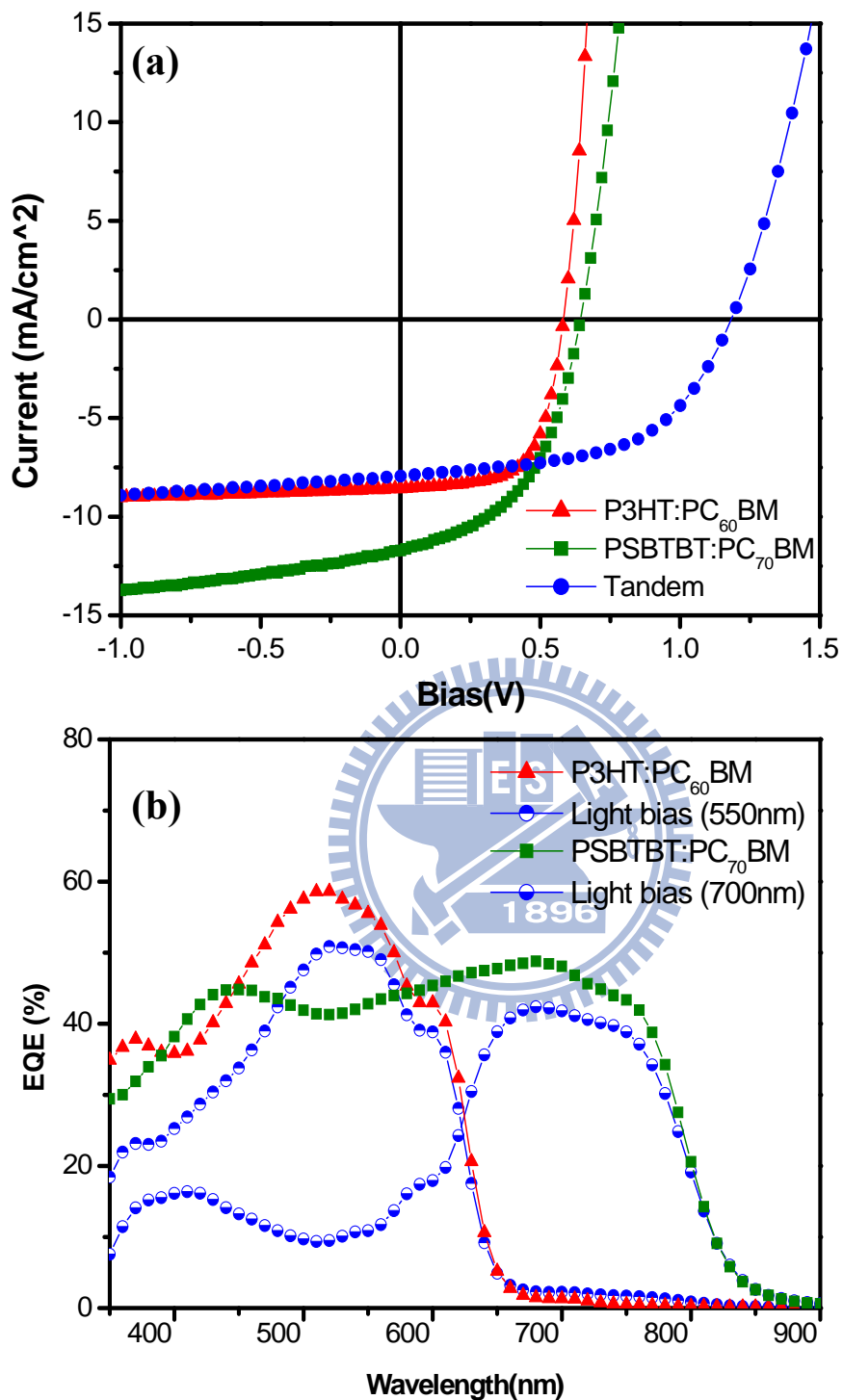**Figure 5.6 :** (**a**) J–V characteristics of a tandem and reference single cells measured under standard AM1.5G, 100mW/cm^2 illumination. (**b**) EQE of sub-cells in tandem structure (with and without monocolor light bias) and reference single cells.

When considering the engineering design on the interlayer, several factors need to be considered. An effective interlayer has to possess the following properties: (1) high optical transparency, (2) good electrical contact to both sub-cells, (3) robustness to protect the underlying layers against solvent. It is also important to select a suitable deposition technique which is compatible with the materials used.

For tandem cells with an inverted structure, the sequence of depositing the interlayer has to be reversed, giving rise to new processing issues that need to be solved. ZnO was chosen as the electron collection layer for both the bottom and top sub-cells based on its stability and ease of processing. Highly efficient ZnO-based single inverted devices have been demonstrated via interfacial modification[95,96]However, the methods above are complicated to apply in the interlayer. For sol-gel processed ZnO using zinc acetate ($Zn(OAc)_2$) as precursor, temperature as high as 300°C is needed to complete the thermal decomposition of the zinc acetate and even higher temperature is needed for the formation of crystals[97']. This temperature is also too high to be used in the processing of the interlayer as it will have detrimental effects to the polymer at the bottom sub-cell. The highest allowable processing temperature would be 150°C without causing serious phase separation or degradation to the polymer blend. At this temperature, the solvent, 2-methoxyethanol, will be evaporated, but the formation of ZnO will not be completed leaving behind ZnO:organic derivatives (ZnO-d) as products[98]. Nevertheless, single inverted devices were fabricated using this hybrid ZnO-d film

to test its effectiveness as the electron collection layer has inconceivable performance with higher fill factor. The dark I-V characteristics of two devices fabricated with the ZnO-d and ZnO films are shown in Figure 5.7(c) and device performance were summarized in Table 5-1. The ZnO-d device exhibited very good diode characteristics with high rectification ratio, and surprisingly, an even lower leakage current than the device with the crystalline ZnO film. The SEM images are shown surface morphology of the ZnO-d and ZnO films. The ZnO-d film was smooth and dense while the ZnO film was more porous.
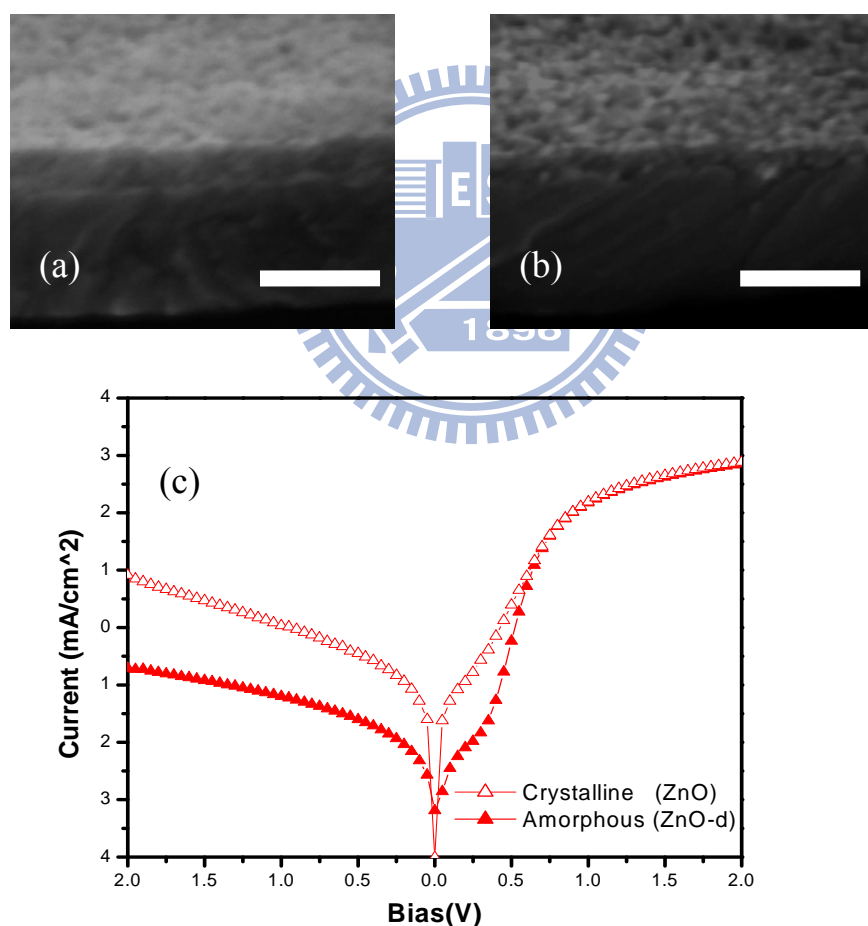

Figure 5.7: FE-SEM cross section images of ZnO on ITO with different annealing temperature (a) $150^{o}C$ and (b) $300^{o}C$; (c) Dark J-V curves of the amorphous ZnO layer (solid triangle) and crystalline ZnO layer (triangle) devices.

Table 5-1 The device performance of inverted cells containing w/ amorphous and w/crystalline ZnO layer.

ZnO annealing temperature	Active Polymer	Voc (V)	Jsc (mA/cm^2)	PCE (%)	FF (%)	R_s/Ω (cm^2)	R_p/Ω (cm^2)
300	P3HT:PCBM	0.58	8.51	2.83	57.5	1.6	700
150	P3HT:PCBM	0.58	8.57	3.17	63.8	1.6	1400
300	P3HT	0.70	0.31	0.1	46.4	22	1400
150	P3HT	0.76	0.24	0.09	50.4	18	1400

The voids in the ZnO film were probably formed during the decomposition of the $Zn(OAc)_2$. Although the ZnO-d film is amorphous, as shown by TEM electron diffraction in Figure.5.5 (a), it did not affect the series resistance of the device. The smooth and compact film of ZnO-d suppressed carrier loss through leakage paths in the film, leading to high FF of 64% in the single-cell device. In order to apply this dense film to as one layer of interlayer, at the same time, being blocking solvent penetration during the deposition of the polymer film of the top sub-cell. How to select the P type material on the first active polymer with the following dense film layer is critical issue.

As demonstrated earlier[99], p-type V_2O_5 and MoO_3 can be used as effective hole collection layer for inverted polymer solar cells without harming prior-deposited organic layers and efficiently improve the performance, compared to use PEDOT:PSS[100]. In the case for our inverted tandem cell, by reducing the thickness of Al of bottom cell to be interlayer with ZnO-d has the advantages of improving the wettability, forming Ohmic contacts and

providing additional recombination sites.[101],[102] The good electrical interfacial contact and chemical compatibility is able to prevent penetration of subsequently deposited layer, collecting electrons and blocking holes with high selectivity.

This is critical to preserve high performance tandem cells. As illustrated in Fig. 5.8, the single device with MoO_3/Al/ZnO-d and MoO_3/ZnO-d as the electron collection layer represents the top halves of a tandem cell, respectively. The device with the Al layer showed a lower leakage current, indicating the better coverage and film quality of the ZnO-d layer. Table 5-2 shows two kinds of active polymer layer fabricated on it and their device performance. On the other hand, Figure 5.9 shows a more dense coverage of ZnO layer is formed using low temperature annealing.
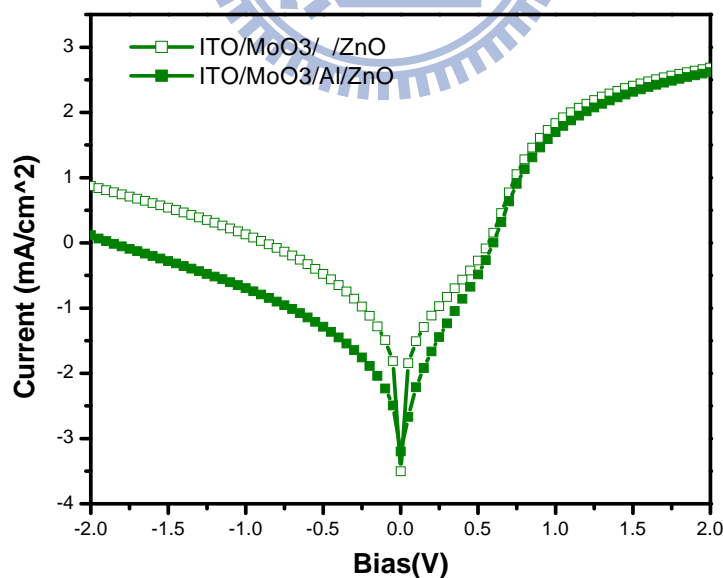

Figure 5.8 : Dark J-V curves of the ITO/MoO_3/Al/ZnO layer (solid square) and ITO/MoO_3/ZnO layer (square) devices.

Table 5-2 Comparison of the device performance of different combined layers on ITO based inverted cells

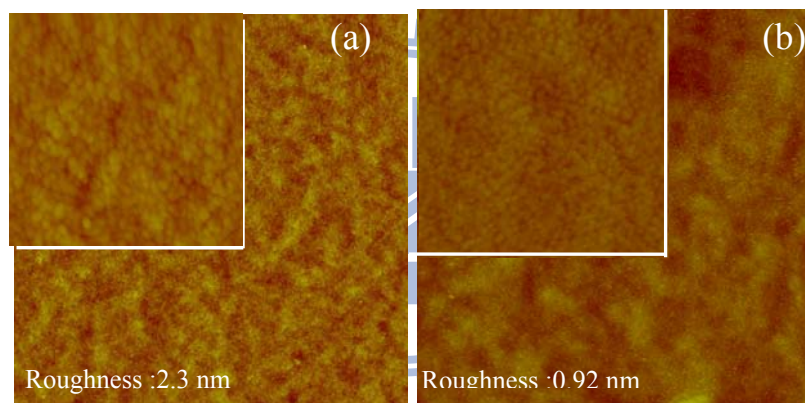| Bottom layer	Active Polymer	Voc (V)	Jsc (mA/cm^2)	PCE (%)	FF (%)	R_p/Ω (cm^2)	R_s/Ω (cm^2)
MoO$_3$/Al/ZnO	P3HT : PCBM	0.58	8.32	3.11	64.3	2.4e^5	23
ZnO	P3HT : PCBM	0.58	8.57	3.17	63.8	3e^6	27
MoO$_3$/Al/ZnO	H-Si : PCBM	0.62	12.4	3.74	48.7	1.3e^5	25
MoO$_3$/ /ZnO	H-Si : PCBM	0.60	13.7	3.81	46.3	2.6e^4	20
ZnO	H-Si : PCBM	0.62	12.6	3.45	44.2	1.4e^5	23

Figure 5.9 : (a) AFM image of ZnO films on top of ITO at 150°C treatment and **(b)** on the top of MoO$_3$/Al with 150oC treatment, respectively. A more dense coverage of ZnO layer is formed.

As a result of the tandem cells with PEDOT/ZnO-d; V$_2$O$_5$/Al/ZnO-d and MoO$_3$/Al/ZnO-d interlayers were fabricated. I-V curves and SEM image are shown in Figure 5.10 where the device with MoO$_3$ showed excellent photovoltaic behavior and clean individual layer stacking, while the one with V$_2$O$_5$ shows an s-shape in the fourth quadrant

that can be attributed to strong interfacial dipole[103]. This interfacial dipole is likely to be formed between the V_2O_5 and ZnO-d interface. The origin of the dipole is still not known but it is likely due to the incompatible chemistry during the hydrolysis of the $Zn(OAc)_2$ which produces acidic residues and MEA as the basic media[104].

In addition, the optical and chemical properties of V_2O_5 are not good to be an effective interlayer. As shown in Figure 5.11, the absorption of V_2O_5 in UV-Vis region will reduce the incident light and react with precursor solution, V_2O_5 is an amphoteric oxide which reacts with both strong non-reducing acids and strong alkali. On the other hand, MoO_3 are acidic in nature and dissolves in water over the neutral to alkaline pH range.[105] The chemical instability of V_2O_5/Al/ZnO interlayer has no function as similar as the Al/ZnO in the inverted tandem cell. Therefore, this interlayer really acts as the a critical role in our inverted tandem structure, the functions of efficient charge recombination, good electrical contact for connection, high transparency and prevention of layer mixing.

Table 5-3 Comparison of device performance of inverted tandem cells with different combined interlayers.

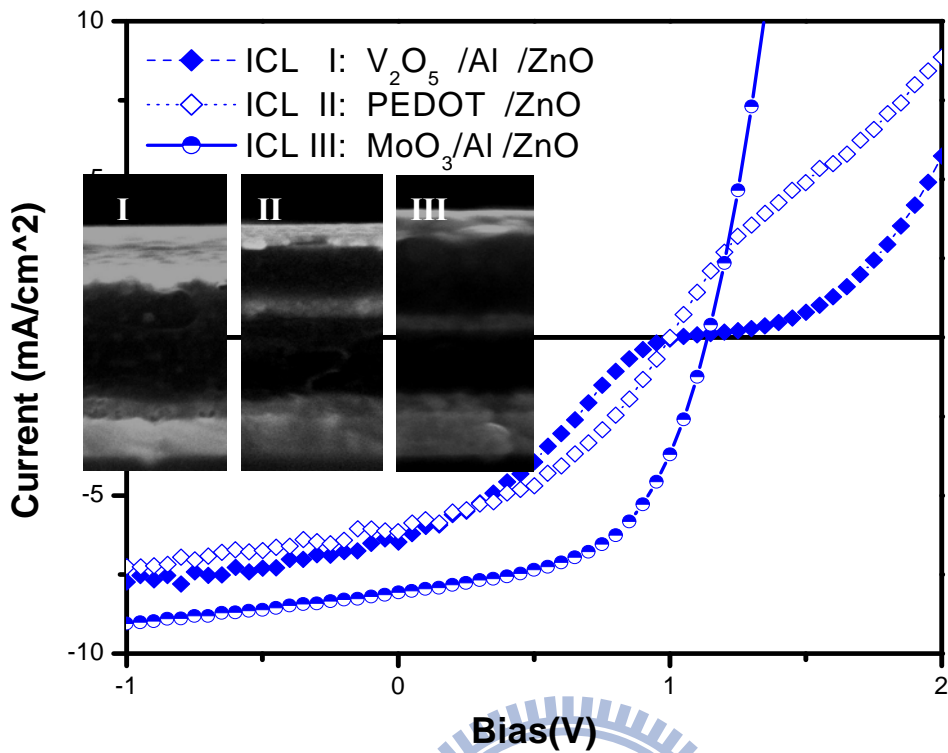| Interlayer	Voc (V)	Jsc (mA/cm²)	PCE (%)	FF (%)
I : V_2O_5/Al/ZnO-d	1.05	6.47	1.97	29.0
II: PEDOT/ZnO-d	1.00	6.14	2.44	39.6
III : MoO_3/Al/ZnO-d	1.20	7.80	5.1	54.1

Figure 5.10 : J–V characteristics of tandem cells with different interlayers. **Insert :** SEM images of each tandem device.
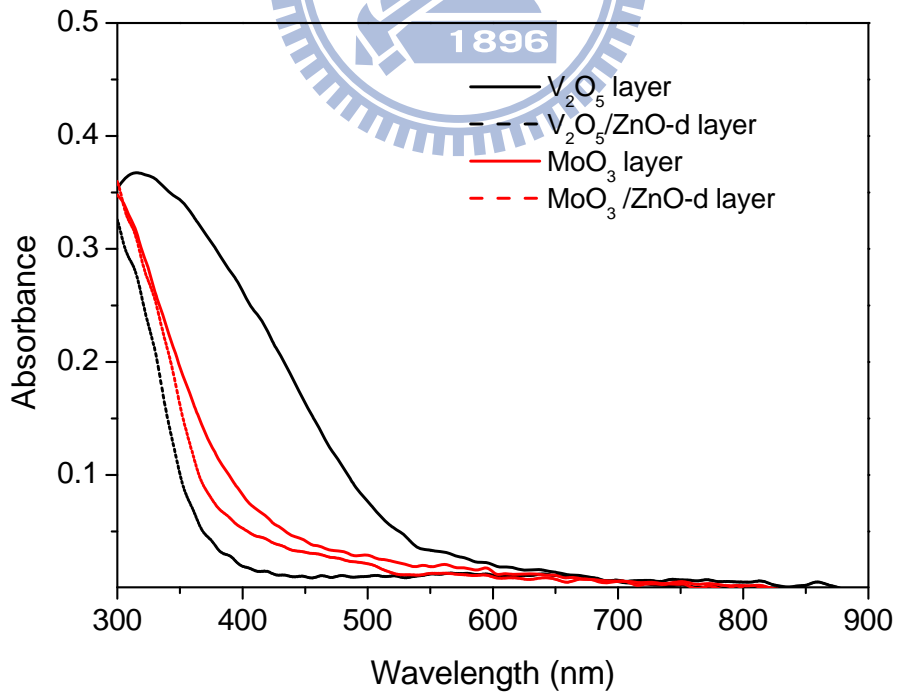

Figure 5.11 : Comparison of the absorption of V_2O_5 and MoO_3 layer before and after ZnO-d deposition.

On the other hand, we demonstrated successfully of the different active polymer applied in MoO$_3$/Al/ZnO interlayer.
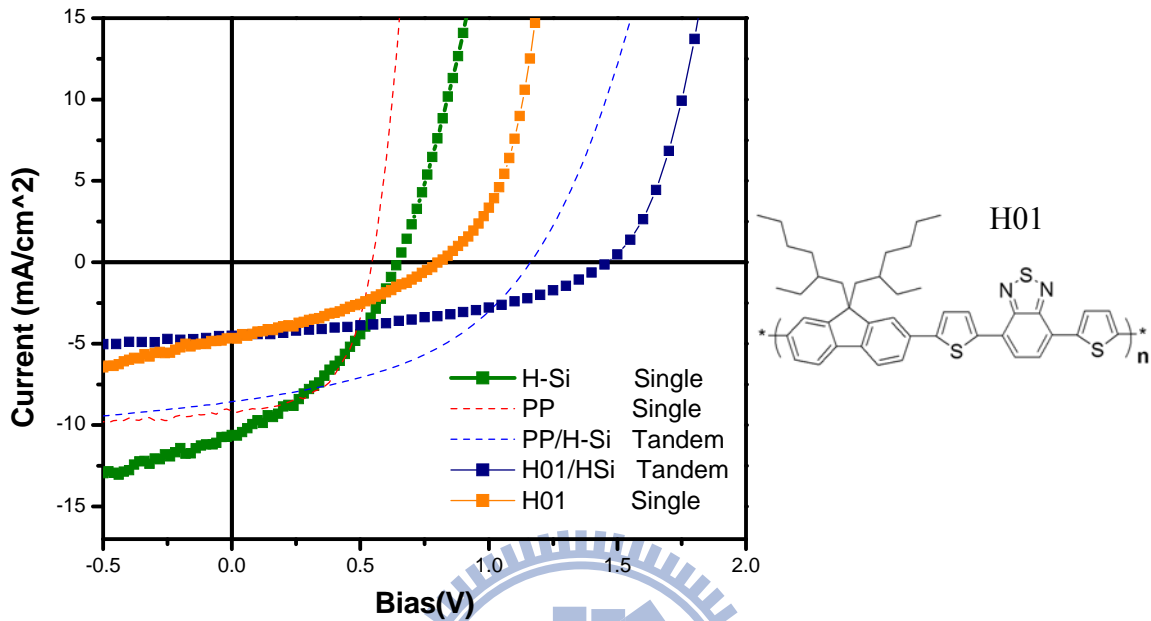

Figure 5.12 : J–V characteristics of tandem cells with different active polymer materials.

The performances of the tandem cells and reference sub-cells under simulated solar illumination of AM 1.5G (100mW/cm^2) are shown in Figure 7.2. The V$_{oc}$ of the tandem cell is equal to the sum of the V$_{oc}$ of each sub-cell, confirming the successful coupling of the two cells in series. We believe this effective layer could be applied in various polymer materials and opens the opportunities for multi- stacked tandem solar cells. The further physical and electrical property is worth to be continued.

5.5 Summary and Conclusions

In conclusion, we have demonstrated successfully a highly efficient inverted polymer solar cell. We introduced a transparent, low temperature processable amorphous ZnO-d layer with excellent charge selectivity. This is critical in achieving high FF in our inverted devices. Physical and chemical compatibility with the hole collecting MoO_3 layer was also studied. Good electrical and optical coupling of the two sub-cells are achieved by using the carefully designed MoO_3/Al/ZnO-d layer. This intermediate layer could be applied in various polymer materials and opens the opportunities for multi-stacked tandem solar cells.
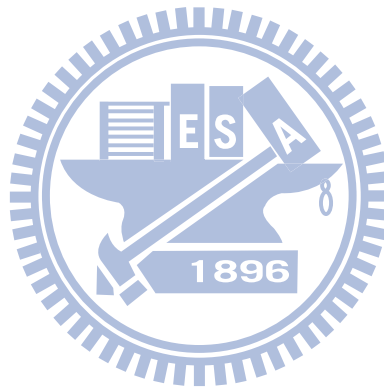
Chapter 6

Conclusions and Future Prospects

6.1 Thesis conclusions

The first part is being the synthesis and characterization of the quantum dot (QD), followed by the fabrication and characterization of the resulting QD-LEDs. We demonstrate that the electroluminescence spectrum can be precisely tuned in diode junction devices in which the mixed color electroluminescence is derived from a yellow emitting QD layers with blue emitting layer PF. Chapter 3 introduces the semiconductor CdSe/ZnS and discusses in detail the synthesis, characterization, and properties, as well as how the application CdSe/ZnS QDs into device. The fabrication and EL characterization of a white-emitting hybrid QD-LED by integrating core-shell CdSe/ZnS QDs acting as a yellow emitter and polyfluorenes as the blue emitter in a multilayered structure.

The second part is being the synthesis and characterization of the zinc oxide (ZnO) materials, followed by the fabrication of the resulting ZnO based polymer solar cells. Chapters 4 discuss the design of a ZnO nano-ridge structured film that can be used as an electron collection layer in an inverted polymer solar cell. The ZnO nano-ridge structure was formed by a simple sol-gel process using a ramp annealing method. As the solvent slowly evaporated due to the low heating rate, there was sufficient time for the gel particles to structurally relax and pile up, resulting in a very dense and undulated film. This film provided an effective charge selection

layer and an increased interfacial area for charge collection. Chapter 5 discusses the study of a

highly efficient tandem polymer solar cell with inverted polarity. The optically transparent

interlayer, consisting of a molybdenum trioxide (MoO_3) layer and an amorphous ZnO, serves

as the interconnecting layer facilitating charge recombination between the bottom and top

sub-cells. The ZnO layer, prepared by a low temperature process, provides a dense layer for

electron collection and a barrier against solvent from dissolving the under layer. The leads to

the high photovoltaic performance in both single and tandem inverted solar cells. Under

simulated solar illumination of AM 1.5G (100 $mWcm^{-2}$), the device exhibited a Jsc = 7.8

$mAcm^{-2}$, Voc = 1.20 V, FF = 0.54, and η = 5.1%.

6.2 Future Prospects

6.2.1 White-Light QD-LED

LEDs with a broad spectral emission generated by electroluminescence from a

mixed-monolayer of red, green, and blue emitting colloidal quantum dots (QDs) in a hybrid

organic/inorganic structure. The goal of the future work is to demonstrate reproducible and

efficient spectrally broad electroluminescent QD-LEDs with spectral emission tunable across

the CIE (Commission Internationale de l'Eclairage) color space.

### 6.2.2 ZnO Nano-Ridge Structure and Its Application in Solar Cells

This novel Nanostructure is easy to fabricate and grow under low temperature. We

believe that using SAM or the two-step nanorod growth could be improved the device
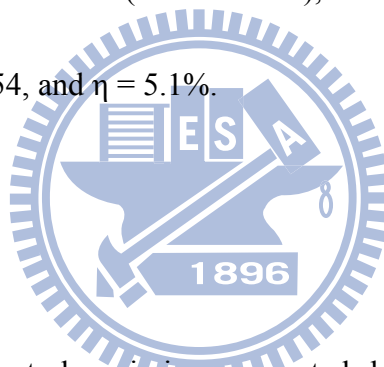
performance. By growing nanorod on nano-ridge, we believe the longer and disorder ZnO nanorod, could provide another way to apply this nanostructure in different energy filed. For example, a relatively new class of photovoltaic devices with a photoelectrochemical system consisting of a dye-sensitized semiconductor film and an electrolyte, dye-sensitized solar cells (DSSCs) is also regarded as a promising alternative.

6.2.3 ZnO-Based Inverted Tandem Polymer Solar Cell

The investigation into this topic could be carried out by three aspects. (1) The mobility of amorphous ZnO. (2) The electrical property of interlayer by using Transient spectra. (3) The applications of interlayer on various polymer materials.
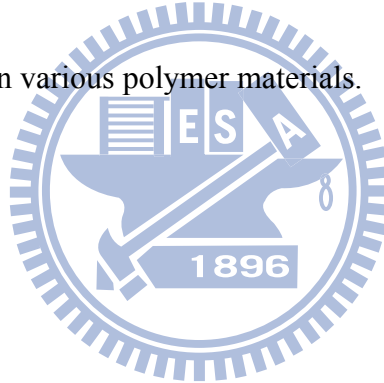
Curriculum Vitae

Cheng-Hsuan (Bruce) Chou

National Chiao Tung University,

Hsinchu, 300, Taiwan

EDUCATION

- **Ph.D**   2004-2009

Department of Applied Chemistry, National Chiao Tung University, Hsinchu, Taiwan

Thesis: The Synthesis and Characterizations of II-VI Semiconductor Nano Materials and
Their Application in Optoelectronic Devices

Advisor: T.M Chen

- **Visiting Scholar** 2008-2009

Department of Materials Science and Engineering, University of California at Los Angeles, USA

- **M.S**   2002-2004

Department of Chemistry and Biochemistry, National Chung Cheng University, Chia-Yi, Taiwan

Thesis: Highly Efficient, Wavelength-Tunable, Gold Nanoparticle Based Optothermal
Nanoconvertors

Advisor: **C. R. Chris Wang**

- **B.A**   1998-2002

Department of Chemistry, Tung Hai University, Taichung, Taiwan

EXPERIENCE

Teaching Assistant

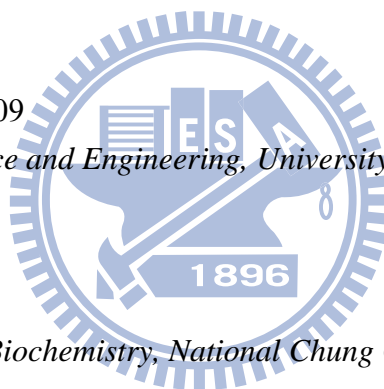2005-2006: National Chiao Tung University, Hsinchu, Taiwan

Courses taught:

* Experimentation of Inorganic Chemistry

2002-2004: National Chung Cheng University, Chia-Yi, Taiwan

Courses taught:

* Physical Chemistry

* TEM Operator

SKILLS

Languages: Fluent in oral and written Chinese, English.

Computer.: Origin, SigmaPlot, SciFinder Scholar.

Specializedl Skills: Microscopy (Atomic Force Microscopy, Transmission Electron Microscopy),

basic spectroscopic techniques, chemical analysis (Nuclear Magnetic

Resonance, Thermal Gravimetric Analysis, X-ray Powder Diffraction),

advanced air-free chemical synthesis techniques.

PUBLICATIONS

[1]**Cheng-Hsuan Chou**, Cheng-Dah Chen, and C. R. Chris Wang*, Highly Efficient, wavelength -Tunable, Gold Nanoparticle Based Optothermal Nanoconvertors. *J. Phys. Chem. B* 109,11135-11138 (2005)

[2]**Cheng-Hsuan Chou,** Chung-He Yang, Chain-Shu Hsu, Teng-Ming Chen*, Hybrid White-Light Emitting-LED Based on Luminescent Polyfluorene Polymer and Quantum Dots. *Journal of Nanoscience and Nanotechnology* 7, 2785–2789 (2007)

[3] Chung-He Yang, Chetan Jagdish Bhongale, **Cheng-Hsuan Chou,** heng-Hsiung Yang, Chih-Nan Lo, Teng-Ming Chen, Chain-Shu Hsu*, Synthesis and light emitting properties of sulfide-containing polyfluorenes and their nanocomposites with CdSe nanocrystals: A simple process to suppress keto-defect. *Polymer* 48, 116-128 (2007)

[4] C.W. Lee, **C.H. Chou**, J.H. Huang, C.S. Hsu and T.P. Nguyen Investigations of organic light emitting diodes with CdSe(ZnS) quantum dots *Materials Science & Engineering B*, 147, 307 (2008)

[5] Nobuyuki Sekine, **Cheng-Hsuan Chou**, Wei Lek Kwan and Y. Yang ZnO nano-ridge structure and its application in inverted polymer solar cell *Organic Electronics* (2009) accecpted.

[6] **Cheng-Hsuan Chou**, Wei Lek Kwan, Ziruo Hong, Li-Min Chen, Yang Yang* Highly efficient inverted polymer tandem solar cells. (2009) *Adv Mater*, submit..

PATENTS

* Patent pending on novel chemistry to create ZnO nano-ridge structure and its applications
* Patent pending on novel chemistry to create Highly efficient inverted tandem polymer solar cell.

Reference

[1] L. E. Brus, *J. Chem. Phys.* **1983**, *79,* 5566.

[2] K. H. Hellwege, L andolt-BornsteinN umericalD ata and FunctionalR elationships in Science and Technology (Springer-Verlag, Berlin, **1982**).

[3] M. A. Kastner, *Physics Today* **1993,** *46,* 24.

[4] C. B. Murray, D. J. Norris, M. G. Bawendi, *J. Am. Chem. Soc.* **1993,** *115,* 8706.

[5] Y.-W. Cao, U. Banin, *Angew. Chem. Int. Ed.* ***1999,*** *38,* 3692.

[6] S. A. Empedocles, M. G. Bawendi, *Acc. Chem. Res.* ***1999,*** *32,* 389.

[7] J. H. Burroughes, D. D. C. Bradley, A. R. Brown, R. N. Marks, K. MacKay, R. H. Friend, P. L. Burn, A. B. Holmes, *Nature* **1990,** *347,* 539

[8] N. C. Greenham, R. H. Friend, *Solid State Phys.* **1995,** *49,* 1.

[9] C. Adachi, M. A. Baldo, S. R. Forrest, S. Lamansky, M. E. Thompson, R. C. Kwong, *Appl. Phys. Lett.* **2001**, *78,* 1622

[10] S. Moller, S. R. Forrest, *J. Appl. Phys.* **2002,** *91,* 3324.

[11] M. Ben Khalifa, D. Vaufrey, J. Tardy, *Org. Electr.* **2004,** *5,* 187.

[12] Z. D. Popovic, H. Aziz, N.-X. Hu, A.-M. Hor, G. Xu, *Synth. Metal.* **2000,** *111,* 229.

[13] S. Dirr, A. Bohler, S. Wiese, H.-H. Johannes, W. Kowalsky, *Jap. J Appl. Phys Part 1-.Regular Papers Short Notes & Review Papers* **1998,** *37,* 1457

[14] C. W. Tang, S. A. VanSlyke, *Appl. Phys. Lett.* **1987,** *51,* 913.

[15] M. A. Baldo, D. F. O'Brien, M. E. Thompson, S. R. Forrest, *Phys. Rev. B* **1999,** *60,* 14422.

[16] V. Bulovic, V. B. Khalfin, G. Gu, P. E. Burrows, D. Z. Garbuzov, S. R. Forrest, *Phys. Rev. B* **1998,** *58,* 3730.

[17] C. A. Leatherdale, C. R. Kagan, N. Y. Morgan, S. A. Empedocles, M. A. Kastner, M. G. Bawendi, *Phys. Rev. B* **2000,** *62,* 2669

[18] V. 1. Klimov, D. W. McBranch, *Phys. Rev. Lett.* **1998,** *80,* 4028.

[19] S. C. Sullivan, W. Woo, J. Steckel, M. Bawendi, and V. Bulovic, *Organic Electronics* **2003,** *4,* 123.

[20] Brabec, C. J., Sariciftci, N. S. & Hummelen, J. C. *Adv. Funct. Mater.* **2001,** *11,* 15.

[21] Coakley, K. M. & McGehee, M. D. *Chem. Mater.* **2004,** *16,* 4533.

[22] Yu, G.,Gao, J., Hummelen, J. C., Wudl, F. & Heeger, A. J. *Science* **1995,** *270,* 1789.

[23] S. S.g Sun, N. S. Sariciftci. *Organic photovoltaics: mechanism, materials, and devices* **2005,** 2th edition**.**

[24] G. Li, V. Shrotriya, J. Huang, Y. Yao, T. Moriarty, K. Emery, and Y. Yang, *Nat. Mater*. **2005,** *4,* 864.

[25] M. L. Ma, C. Y. Yang, X. Gong, K. Lee, and A. J. Heeger, *Adv. Funct. Mater.* **2005,** *15,* 1617.

26 J. Peet, J. Y. Kim, N. E. Coates, W. L. Ma, D. Moses, A. J. Heeger, and G. C. Bazan, *Nat. Mater.* **2007,** *6***,** 497.

27 J. Hou, H. Y. Chen, S. Zhang, G. Li, and Y. Yang, *J. Am. Chem. Soc.* **2008,** *130*, 16144.

28 C. J. Brabec, J. A. Hauch, P. Schilinsky, C. Waldauf, *MRS Bull.* **2005**, *30*, 50.

29 V. D. Mihailetchi, P. W. M. Blom, J. C. Hummelen, M. T. Rispens, *J. Appl Phys.* **2003**, *94*, 6849.

30 J. Y. Kim, K. Lee, N. E. Coates, D. Moses, T.-Q. Nguyen, M. Dante, A. J. Heeger, *Science* **2007**, *317*, 222.

31 Y.K. Kim, K.Y. Lee, O.K. Kwon, D.M. Shin, B.C. Sohn, J.H. Choi. *Synth Met* **2000**,*111*, 207.

32 K. Lee, N.S. Sariciftci, A.J. Heeger. *Synth Met* **1995,** *69*,445.

33 J.H. Park, Y.T. Lim, O.O. Park, J.K. Kim, J.W. Yu, Y.C. Kim. *Chem Mater* **2004**.*16*, 688.

34 C.W. Lee, C.H. Chou, J.H. Huang, C.S. Hsu and T.P. Nguyen *Materials Science & Engineering B*, 147, 307 (2008)

35 C.H. Chou, H.S. Wang, K.H. Wei, J.Y. Huang. *Adv Funct Mater* **2006**,*16*, 909.

36 K.B. Chen, M.H. Chen, S.H. Yang, C.H. Hsieh, C.S. Hsu, C.C. Chen. *J Polym Sci Part A Polym Chem* **2006**, *44*, 5378.

37 C.H. Yang, C. J. Bhongale, C. H. Chou, H.H. Yang, C.N. Lo, T. M. Chen, C. S. Hsu, *Polymer* **2007,** *48*, 116.

38 J. H. Park, J. Y. Kim, B. D. Chin, Y. C. Kim, J. K. Kim and O. O. Park, *Nanotechnology* **2004,** *15*, 1217.

39 P. Reiss, J. Bleuse and A. Pron, *Nano Lett.* **2002,** *2*, 781.

40 Z. A. Peng and X. Peng, *J. Am. Chem. Soc.* **2001**, *123*, 184.

41 A. A. Shoustikov, Y. You and M. E. Thomson, *IEEE J. Sel. Top. Quantum Electron.* **1998** *4*, 3.

42 M. C. Schlamp, X. Peng and A. P. Alivasators, *J. Appl. Phys.* **1997,** *82***,** 5837.

43 S. C. Sullivan, W. Woo, J. Steckel, M. Bawendi, and V. Bulovic, *Adv. Funct. Mater.* **2005**, *15*, 1117

44 B. O. Dabbousi, M. G. Bawendi, O. Onitsuka, M. F. Rubner, *Appl. Phys. Lett.* **1995**, *66,* 1361.

45 H. Mattoussi, L. H. Radzilowski, B. O. Dabbousi, D. E. Fogg, R. R. Schrock, E. L. Thomas, M. F. Rubner, M. G. Bawendi, *J. Appl. Phys.* **1999,** *86***,** 4390.

46 V. L. Colvin, M. C. Schlamp and A. P. Alivasators, *Nature* **1994**, *370*, 354.

47 M. C. Schlamp, X. Peng and A. P. Alivasators, *J. Appl. Phys.* **1997,** *82*, 5837.

48 M. P. de Jong, L. J. van Ijzendoom, M. J. Ad. Voigt, *Appl. Phys. Lett.* **2000**, *77*, 2255.

49 S. K. Hau, H. L. Yip, N. S. Baek, J. Zou, K. O'Malley, and A. K. Y. Jen, **Appl. Phys. Lett. 2008,** *92***,** 253301.

50 L.M. Chen, Z. Hong, G. Li, Y. Yang. *Adv Mater* **2009,** *21,* 1434.

[51] Z. Xu, L. M. Chen, G. W. Yang, C. H. Huang, J. Hou, Y. Wu, G. Li, C. S. Hsu, Y. Yang. *Adv. Funct. Mater.*, **2009**, *19*, published online.

52 G. Li, C. W. Chu, V. Shrotriya, J. Huang, and Y. Yang, *Appl. Phys. Lett.* **2006**, *88*, 253503

53 H. H. Liao, L. M. Chen, Z Xu, G. Li, and Y. Yang, *Appl. Phys. Lett*. **2008**, *92*, 173303.

[54] M. S. White, D. C. Olson, S. E. Shaheen, N. Kopidakis, and D. S. Ginley, *Appl. Phys. Lett*. **2006**, *89*, 143517.

[55] A. K. K. Kyaw, X. W. Sun, C. Y. Jiang, G. Q. Lo, D. W. Zhao, and D. L. Kwong, *Appl. Phys.* Lett. **2008**, *93*, 221107.

[56] C. Waldauf, M. Morana, P. Denk, P. Schilinsky, K. Coakley, S. A. Choulis, C. J. Brabec, Appl. Phys. Lett. **2006**, *89*, 233517.

[57] G. K. Mor, K. Shankar, M. Paulose, O. K. Varghese, C. A. Grimes, *Appl. Phys. Lett.* **2007**, *91*, 152111.

[58] S. Bandyopadhyay, G.K. Paul, S.K. Sen, *Sol. Energy Mater. Sol. Cells* **2002**, *71*, 103.

[59] Y. Natsume, H. Sakata, *Thin Solid Films* **2000**, *372*, 30.

[60] P. Nunes, D. Costa, E. Fortunato, R. Martins, *Vacuum* **2002**, *64*, 293.

[61] D.C. Look, D.C. Reynolds, C.W. Litton, R.L. Jones, D.B. Eason, G. Gantwell, *Appl. Phys. Lett.* **2002**, *81*, 1830.

[62] K. Tominaga, T. Takao, A. Fukushima, T. Moriga, I. Nakabayashi, *Vacuum* **2002**, *66*, 505.

[63] N. Naghavi, C. Marcel, L. Dupont, A. Rougier, J.B. Leriche, C. Guery, *J. Mater. Chem.* **2000**, *10*, 2315.

[64] M. Krunks, E. Mellikov, *Thin Solid Films* **1995**, *270*, 33.

[65] T. Shuler, M.A. Aegerter, *Thin Solid Films* **1999**, *351*, 125.

[66] Y. Natsume, H. Sakata, Mater. Chem. Phys. **2002**, *78*, 170.

[67] E.J. Luna-Arredondo, A. Maldonado, R. Asomoza, D.R. Acosta, M.A. Melendez-Lira, M. de la L. Olvera, *Thin Solid Films* **2005**, *490*, 32

[68] N.R.S. Farley, C.R. Staddon, L.X. Zhao, K.W. Edmunds, B.L. Gallagher, D.H. Gregory, *J. Mater. Chem*. **2004**, *14*, 1087.

[69] N. Viart, M. Richard-Plouet, D. Muller, G. Pourroy, *Thin Solid Films* **2003**, *437*, 1.

[70] A.E. J.-Gonzalez, J.-A. S.-Urueta, R. S.-Parra, *J. Cryst. Growth* **1998**, *192*, 430.

[71] L.J. Mandalapu, F.X. Xiu, Z. Yang, D.T. Zhao, J.L. Liu, *Appl. Phys. Lett*. **2006**, *88*, 112108.

[72] B.S. Ong, C. Li, Y. Li, Y. Wu, R. Loutfy. *J. Am. Chem. Soc.* **2007**, 129, 2750.

[73] M. S. White, D. C. Olson, S. E. Shaheen, N. Kopidakis, and D. S. Ginley, *Appl. Phys. Lett*. **2006**, *89*, 143517.

[74] S. K. Hau, H. L. Yip, Hong Ma. and A. K. Y. Jen, *Appl. Phys. Lett*. **2008**, *93*, 233304.

[75] DC Olson, SE Shaheen, RT Collins, DS Ginley *J. Phys. Chem. C* **2007**, *111*, 16670.

[76] K. Takanezawa, K. Hirota, Q. S. Wei, K. Tajima, and K. Hashimoto, *J. Phys. Chem. C* **2007**, *111*, 7218.

[77] M. Ohyama, H. Kozuka, and T. Yoko, *Thin Solid Films* **1997,** *306***,** 78.

[78] G. Li, C. W. Chu, V. Shrotriya, J. Huang, and Y. Yang, *Appl. Phys. Lett.* **2006,** *88*, 253503.

[79] R. D. Deegan , O. Bakajin, T. F. Dupont, G. Huber, S. R. Nagel and T. A. Witten *Nature* **1997,** *389***,** 827.

[80] E. Rabani1, D. R. Reichman, P. L. Geissler, and L. E. Brus, *Nature* **2003,** *426***,** 271.

[81] Y. S. Kim, W.P. Tai, S. J. Shu, *Thin Solid Films* 2005, *491*,153.

[82] D.C. Olson, S.E. Shaheen, R.T. Collins, D.S. Ginley *J. Phys. Chem. C* **2007,** *111*, 16670.

[83] A. Hadipour, B. de Boer, P.W.M. Blom. *Organic Electronics* **2008,** *9*, 617.

[84] J. Y. Kim, K. Lee, N. E. Coates, D. Moses, T.-Q. Nguyen, M. Dante, A. J. Heeger, *Science* **2007**, *317*, 222.

[85] J. Gilot, M. M. Wienk, R. A. J. Janssen, *Appl. Phys. Lett.* **2007**, *90*, 143512.

[86] A Hadipour, B de Boer, PW Blom, *Adv. Funct. Mater.* **2008**, *18*, 169

[87] S. Sista, M.H. Park, Z. Hong, Y. Wu, J. Hou, W. L. Kwan, G. Li, Y.Yang, *Adv. Mater.* **2009**, published onlin*e*

[88] H. H. Liao, L. M. Chen, Z Xu, G. Li, Y. Yang, *Appl. Phys. Lett.* **2008,** 92, 173303.

[89] C. Waldauf, M. Morana, P. Denk, P. Schilinsky, K. Coakley, S. A. Choulis, C. J. Brabec, *Appl. Phys. Lett*. **2006**, 89, 233517

[90] M.-H. Park, J.-H. Li, A. Kumar, G. Li, Y. Yang, *Adv. Mater.* 2**009**, *19*, 1241

[91] M. S. White, D. C. Olson, S. E. Shaheen, N. Kopidakis, D. S. Ginley, *Appl. Phys. Lett*. **2006**, 89, 143517.

[92] L.-M. Chen, Z. Hong, G. Li, Y. Yang, *Adv. Mater*. **2009**, 21, 1434.

[93] T. Ameri, G. Dennler, C. Lungenschmied, C.J. Brabec, *Energy Environ. Sci.*, **2009**, *2*, 347.

[94] J. Hou, H.-Y. Chen, S. Zhang, G. Li, Y. Yang, *J. Am. Chem. Soc*. **2008**, 130, 16144

[95] S. K. Hau, H. L. Yip, N. S. Baek, J. Zou, K. O'Malley, and A. K. Y. Jen, *Appl. Phys. Lett.* **2008,** *93***,** 233304.

[96] K. Takanezawa, K. Tajima, and K. Hashimoto, *Appl. Phys. Lett*. **2008,** *93*, 063308.

[97] B.S. Ong, C. Li, Y. Li, Y. Wu, R. Loutfy. *J. Am. Chem. Soc.* **2007**, 129, 2750.

[98] H. Li, J. Wang, H. Liu, C. Yang, H. Xu, X. Li, H. Cui, *Vacuum,* **2004,** 77, 57.

[99] V. Shrotriya, G. Li, Y. Yao, C.-W. Chu, Y. Yang, *Appl. Phys. Lett.* **2006**, 88, 073508.

[100] A. K. K. Kyaw, X. W. Sun, C. Y. Jiang, G. Q. Lo, D. W. Zhao, and D. L. Kwong, Appl. Phys. Lett. 93, 221107 (2008)

[101] H.K. Kim, K.K. Kim, S.J. Park, T.Y. Seong, I. Adesida *J. Appl. Phys*. **2003,** *94*, 4225.

[102] A. Yakimov, S. R. Forrest, *Appl. Phys. Lett*. **2002**, *80*, 1667.

[103] A Kumar, S Sista, Y Yang *J. Appl. Phys.* **2009**, *105***,** 094512.

[104] M. Ohyama, H. Kozuka, T. Yoko, *Thin Solid Films* **1997**, *306***,** 78.

[105] N. N. Greenwood, A. Earnshaw, *Chemistry of the Elements, 2nd ed.*, **1997**, Butterworth-Heinemann, Oxford, UK.